RADIO SCIENCE, VOL. 48, 69–88, doi:10.1002/rds.20022, 2013

Efficiency enhancement of single off-axis and multiple overlapping beam reflectors using dielectric-covered focal plane array feeds

M. Ng Mou Kehn[1]

Received 6 August 2012; revised 3 December 2012; accepted 6 February 2013; published 1 March 2013.

[1] Reflector antennas fed by dense focal plane arrays (FPAs) are known for their high aperture efficiency, low scan loss, and ability to achieve closely overlapping beams and thus improved continuity in the field of scan. These benefits are possible because FPAs comprise electrically small elements with diameters within half a wavelength, which sample the focal plane fields to a high resolution. This work explores the prospects of further enhancing the total efficiency of FPA-fed reflector systems by using dielectric covers placed over FPA feeds composed of open-ended waveguides. The parameters investigated are the permittivity and thickness of the dielectric layer. We will demonstrate the ability of these covers to improve the overall efficiency of reflectors compared to that of reflectors fed by uncovered FPAs, over several beam widths of scan for single steered beams, as well as to enhance the individual constituent beam efficiencies of simultaneously overlapping multiple beams.

Citation: Ng Mou Kehn, M. (2013), Efficiency enhancement of single off-axis and multiple overlapping beam reflectors using dielectric-covered focal plane array feeds, *Radio Sci.*, *48*, 69–88, doi:10.1002/rds.20022.

1. Introduction

[2] The last decade has seen massive growth in mobile satellite and radio communications [*Hwang*, 1992]. Satellite systems today provide a vast range of services within the commercial and military sectors [*Brisken et al.*, 1979; *Zaghloul et al.*, 1990; *Wu et al.*, 1994]. Due to the high capacity, mobility, and ever-changing geographical distribution of modern users, there is a growing need to generate multiple directive beams that are rapid, robust, and highly reconfigurable [*Egami*, 1987]. Multiple-beam reflector (MBR) antennas are attractive candidates for meeting this demand as they can be launched into orbit to provide numerous spot beams as well as contoured (shaped) footprints [*Balling*, 1987].

[3] There had been keen efforts to improve MBRs, such as the use of dual offset dishes to reduce scan loss and cross-polarization [*Jorgensen and Balling*, 1985]. The capacity of communication satellite systems had been limited by the decreasing amount of available bandwidth. A way around this is to reuse the bandwidth by using spatially isolated antenna beams and/or orthogonal polarizations [*Kreutel et al.*, 1977]. In a bid toward this, hundreds to thousands of spot beams were considered in the work of *Egami* [1999]. This underlines the rising importance of the ability to generate highly efficient overlapping spot beams.

[4] Dense focal plane array (FPA) feeds for MBRs are known for their ability to achieve high aperture efficiency, low scan loss, and closely overlapping beams for extended fields of continuous coverage. Comprising electrically small elements with diameters up to half a wavelength, such versatile array feeds can be excited according to any focal plane field pattern corresponding to a diverse set of beam configurations, be it a single scanned beam or simultaneous multiple beams (closely overlapping or widely separated). Using digital beam-forming networks, such FPA feeds are able to provide rapid and adaptive beams that can be swiftly adjusted to satisfy the needs of dynamically changing environments. Hence, FPA feeds play an important advancing role in today's satellite technology.

[5] There has been a study which showed that dielectric layers placed over FPAs comprising open-ended waveguides can serve as effective impedance match tuners that significantly improve the radiation efficiency of the feed [*Ng Mou Kehn and Shafai*, 2009]. That work, however, only considered axial reflector beams and did not take other subefficiencies characterizing the entire FPA-fed reflector system into account. This motivates further investigations of such dielectric layers over FPAs, but now for improving the overall efficiency encompassing all subefficiencies of the FPA-fed reflector, not only for axial beams but also for off-axis ones, including simultaneously overlapping multiple beams.

[6] The purpose of this paper is thus to look into the prospects of further enhancing the performance of FPA-fed reflectors by placing dielectric matching covers over the FPA feed. Parabolic reflectors were treated, and the FPAs considered here consist of open-ended sidewall loaded hard rectangular waveguides (HRWs), the same type of element

[1]Department of Electrical and Computer Engineering, Institute of Communications Engineering, National Chiao Tung University, Hsinchu, Taiwan.

Corresponding author: M. Ng Mou Kehn, Department of Electrical and Computer Engineering, Institute of Communications Engineering, Engineering Building IV, National Chiao Tung University, 1001 University Road, Hsinchu 30010, Taiwan. (malcolmaxwell@gmail.com)

1944-799X/13/rds.20022

studied by *Ng Mou Kehn and Kildal* [2005]. The amplitude uniformity and polarization linearity of the aperture fields make such waveguides constitutionally suitable as FPA elements. The lateral view of this sheathed waveguide array is shown in Figure 1, and the perspective albeit out-of-scale schematics of the entire FPA-fed reflector system for the two contending configurations— one being the uncovered FPA and the other the dielectric-covered version—are shown in Figure 2. We will demonstrate the ability of dielectric covers to improve the overall efficiency of reflectors over several scan beam widths as compared to those that are fed by uncovered FPAs.

2. Description of the Theory and Formulation: An Overview

[7] With the exception of the embedded element analysis provided in section 3, the mathematical details of the theories and concepts behind the treatment of the present complex reflector antenna system (comprising the dielectric-covered waveguide FPA and the paraboloid itself) can be found in published works by the author (references cited along the way). But for completeness, textual descriptions of various vital parts shall still be conveyed here in a logical order to provide a big picture overview of the vast theoretical framework that is not found anywhere else.

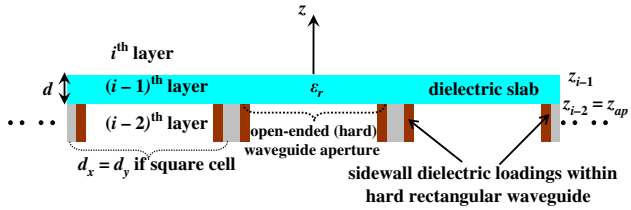

Figure 1. Lateral view of waveguide array covered by a dielectric layer. The rectangular waveguides are sidewall loaded by dielectric slabs, as shown, serving as hard waveguides.

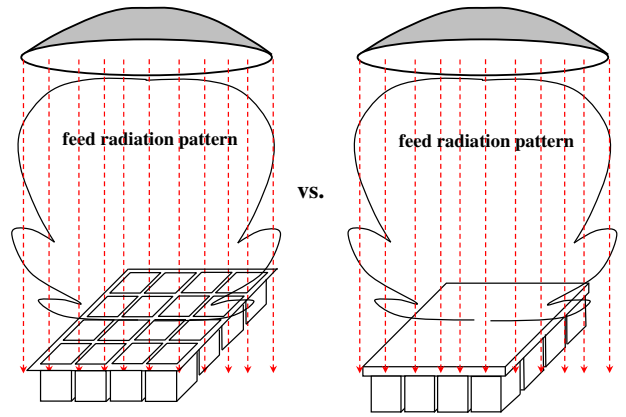

Figure 2. Waveguide FPA feeds for the (a) uncovered reflector and (b) dielectric-covered reflector.

2.1. Dielectric Sheet–Covered Waveguide Array Operated as Phased Array—Auxiliary for Treatment of Arbitrarily Excited Finite Arrays

[8] The details of the analysis and formulation for treating the waveguide array covered by a dielectric layer have been presented by *Ng Mou Kehn and Shafai* [2009]. But for completeness, the method is still textually summarized here. It is first emphasized that the upcoming description pertains to the solution of the dielectric-covered waveguide array when operated as a conventional phased array, i.e., a single fundamental Floquet mode (with an associated forcing wave number) that excites the entire structure, pertaining to the phase-steered beam angle.

[9] The moment method using spectral Green's functions for solving multilayer structures is employed. The core of this latter approach lies in the so-called G1DMULT routine [*Sipus et al*., 1998; *Ng Mou Kehn et al*., 2006], which is self-developed. In addition to the forward incident fields of the dominant waveguide mode, the aperture fields of the waveguides are expanded as a sum of backward reflected waveguide modal fields. In this way, the PEC equivalence magnetic aperture current related to the aperture electric fields is expanded into entire-domain trigonometric waveguide modal basis functions. Each basis current is then Fourier transformed into a certain spectral basis current whose radiated fields under the multilayer environment can be acquired from G1DMULT. Due to the periodicity, in addition to the fundamental Floquet mode defined by the forcing wave number mentioned earlier, a discrete spectrum of higher-order Floquet harmonic plane waves is radiated. Upon summing up all these plane waves, the spatial fields caused by any basis current are obtained. This shall then be repeated for all other basis currents and the respective fields are combined. In this way, the total fields (caused by the array of magnetic current sources) in terms of the amplitude coefficients of the basis functions can be determined.

[10] These fields are then used to enforce the boundary conditions within one unit cell, requiring the continuity of the tangential magnetic field components over the waveguide aperture. Galerkin weighting of the boundary conditions then yields a system of equations that can be solved numerically for the expansion coefficients. Consequently, the active (phased array) reflection coefficient and embedded element patterns along with their radiated powers can be obtained. The concepts and theory behind the latter are given in section 3, thereby elucidating the importance of that section.

[11] The foregoing solution of the phased array scenario can then be used for mutual coupling analysis, the theoretical details of which can be found in the work of *Ng Mou Kehn and Shafai* [2008]. But briefly described here, by repeatedly solving the above-described phased array scenario for the active reflection coefficient over numerous phasings (steered beam directions), which are then integrated over the Brillouin zone, the embedded element mutual coupling coefficients may be acquired. This is based on the classic theorem stating that the active reflection coefficient of the infinite phased array and the coupling coefficient under the embedded element scenario (EES) constitute a Fourier transform pair [*Amitay et al*., 1972]. It is specified further that this coupling coefficient relates the incident dominant (forward-traveling) mode of the excited element to another generally different

(higher-order) backward-traveling mode of any other passive element into which energy is seeped, including the excited element itself (reflection loss). The treatment of arbitrarily excited finite arrays may then ensue using these coupling coefficients, whereby the power loss in any array element is calculated by summing up the mutually coupled modal power losses contributed by all surrounding elements as well as the self-coupling loss, i.e., the reflection loss. Therefore, the solution of the infinite phased array scenario only serves as an auxiliary step for treating the finite array. Also, as explained by *Ng Mou Kehn and Shafai* [2008], there is an alternative validation approach based on the superposition of amplitude-scaled and phase-shifted embedded element patterns according to the location of each element. From both approaches, power balance is satisfied. This underlines the pertinence of the EES, whose analysis is presented in section 3. As mentioned earlier about the incident dominant waveguide mode, it is reiterated that in the present study (for arbitrarily excited finite FPAs in particular), the waveguide elements are always assumed to be excited by the dominant mode, being the LSE symmetric $n=0$ mode [*Ng Mou Kehn and Kildal*, 2005] for inhomogeneously sidewall loaded rectangular waveguides, which reduce to the TE_{10} mode of homogeneous ones when the dielectric walls and the central portion are of the same material. Such injected dominant modes are *y*-polarized for this study. A set of higher-order modes constitutes the backward-traveling waves inside each element.

2.2. Dielectric Sheet–Covered Waveguide Array Operated as FPA Feeds for Reflectors

2.2.1. Focal Plane Field Synthesis by Physical Optics

[12] Now that we have formulated the treatment of arbitrarily excited dielectric sheet–covered waveguide arrays, we next need to know how this arbitrary excitation should be in order for the array to serve as an FPA feed of a parabolic reflector. This is determined by the conventional approach of first synthesizing the fields arising on the focal plane of the paraboloid due to an impingent plane wave arriving from a certain direction (receive mode) using physical optics (PO). When the FPA feed is excited according to this field distribution (on transmit) via conjugate field matching, i.e., by sampling the focal plane fields in a discretized and truncated manner (by the treatment of arbitrarily excited finite arrays as described above), the resultant reflector beam would shine toward that direction of the incoming plane wave. The details of the PO treatment have been provided by *Ng Mou Kehn and Shafai* [2008]. It is worth mentioning that although the focal plane fields of axial incidence take on the approximate but closed form of the Airy ring pattern, there is no likewise analytical function for describing the focal fields of off-axis incidences. Also, it should be pointed out that although the polarization of the incident plane wave is either only *x*-polarized or *y*-polarized, the synthesized focal plane fields contain both co-polar and cross-polar components, with the latter in a smaller proportion. Hence, the FPA elements have to be excited by modes that bear the same polarization as the co-polar focal plane fields. For our present case of *y*-polarized injected modes of waveguide elements, we restrict the investigations to *y*-polarized incident plane waves, although without loss of generality.

[13] To illustrate the mechanism for a parabolic reflector with 60° half-subtended angle (or simply dish angle) and 5 m diameter at 10 GHz, Figure 3 shows the focal plane fields due to *y*-polarized incident plane waves (*xz* plane of incidence) along two directions (0° and 1°) synthesized by the integration of the PO-induced currents over the paraboloid surface. It is to be stated that only the amplitude levels of the complex valued fields are plotted, omitting the phase information, as this just aims to provide a visual feel of the focal plane field distribution. The actual FPA sampling would entail excitation of the array elements by the complex field values. In addition, only the focal plane distribution of the co-polar E_y field component is presented. The fictitiously drawn rays and reflectors just serve to illustrate the skew of the focal point under off-axis incidence and are not to scale.

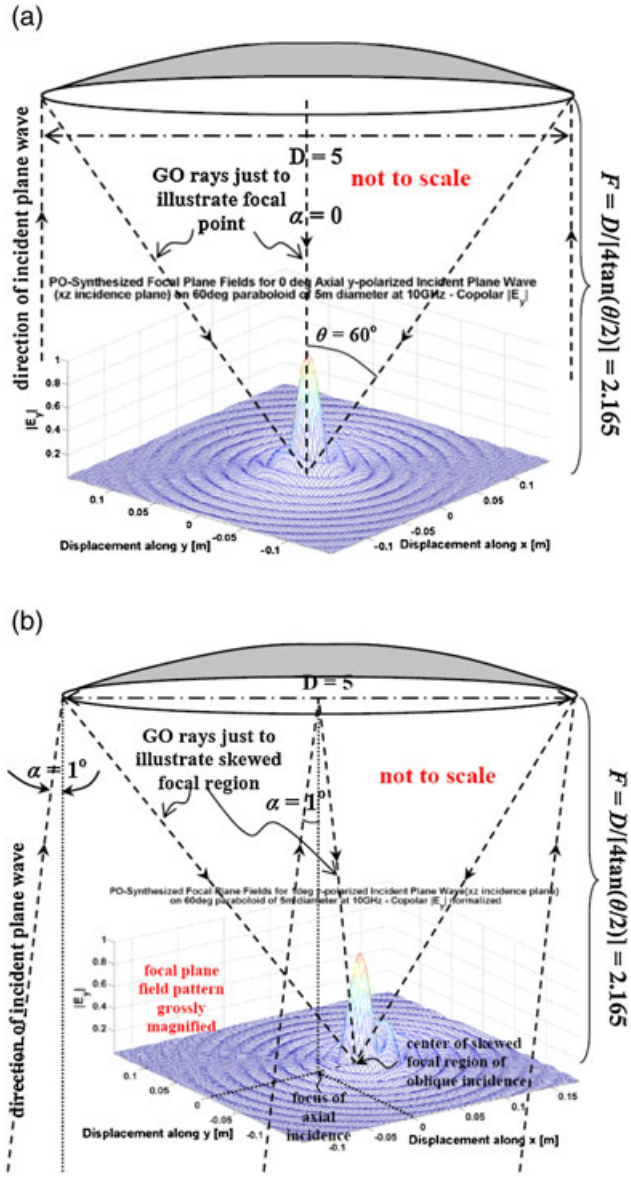

Figure 3. Synthesized focal plane fields by PO integration for 60° dish angle at 10 GHz for *y*-polarized plane wave incidences: (a) axial incidence and (b) 1° off-axis incidence. Amplitude levels are shown (without phase information). Only the co-polar E_y field component is given and the *xz* plane of incidence considered. Focal length F related to diameter D and half-subtended angle θ as indicated.

The beam angle (on transmit) or plane wave incidence angle (on receive, for focal plane field synthesis) shall henceforth be denoted by α, as indicated in Figure 3.

2.2.2. Off-axis Beam Efficiency: Integration Over Tilted Focal Plane Based on Geometrical Optics Projection

2.2.2.1. Feed-radiated fields—superposition of element patterns

[14] When dealing with conventional axial beams, the well-known illumination, polarization, and phase subefficiencies (see section 2.3) of the reflector are calculated by integrating the focal plane fields using classic formulas [*Kildal*, 2000], which are derived by geometrical optics (GO) ray tracing of the feed-radiated fields. These latter emitted fields are, in our FPA case here, obtained by summation of embedded element patterns, with each amplitude scaled and phase shifted according to its respective element location within the synthesized focal plane field distribution outlined in section 2.2. Each element pattern is calculated by the analysis presented in section 3. Hence, the solution of the phased array scenario, obtainable by the approach outlined in section 2.1, is a fundamental building block.

2.2.2.2. GO projection of fields onto tilted elliptical aperture

[15] The abovementioned focal plane for axial beams is perpendicular to the reflector axis, and the domain of integration for subefficiency calculations simply spans over the circular area projected onto the focal plane by the paraboloid along the axial direction. However, for off-axis beams, the aperture over which the field integration is to be performed is now tilted, squished into an ellipse, and perpendicular to the oblique beam direction [*Ng Mou Kehn and Shafai*, 2008]. Therefore, the usual focal plane fields over the untilted aperture (applicable only to axial beams) have to be projected using GO along the axial direction onto the new tilted elliptical focal plane. This is what we call GO-ray continuation. The details of these concepts are available in the work of *Ng Mou Kehn and Shafai* [2008].

2.2.3. Treatment of Overlapping Beams by Superposing Individual Off-axis Beams

[16] Where overlapping beams are concerned, the synthesis of the focal plane fields to be sampled by the FPA can be performed by simply superposing the separately synthesized focal plane fields of the various beam angles involved. In other words, the focal plane fields arising from the plane wave arriving from any beam direction (on receive) are first synthesized individually. Repeating for the other beam directions and then adding up the respective focal plane fields (in both amplitude and phase, i.e., complex value addition) yield the final focal plane field distribution, to be subsequently sampled by the FPA in the usual discretized and truncated manner. The synthesized focal plane fields for 0° and 1° overlapping beams for a 60° paraboloid of 5 m diameter at 10 GHz are shown in Figure 4a, whereas an example of FPA discretized sampling is given in Figure 4b. Only the amplitudes of the complex co-polar E_y field component are presented.

[17] As for the subefficiencies, it is noted that while each configuration of simultaneous beams has certain decoupling and spillover efficiencies, there is one set of aperture subefficiencies (illumination, polarization, and phase efficiencies; see section 2.3) for every constituent beam. The calculation of these subefficiencies for each beam follows the same integration of the GO fields projected onto the tilted elliptical aperture as that for single off-axis beams (as explained in section 2.2.2), but now this is repeated as many times as there are overlapping beams, with each GO-ray projection plus integration being performed over the respective beam's tilted aperture. Hence, although the FPA-radiated fields existing over the untilted focal plane aperture for a particular set of overlapping beams are fixed and common to all beams, the fields existing over the respective tilted apertures are different for various beams, because they are GO projected by different amounts.

2.2.4. Secondary Radiation from Reflector Aperture

[18] The ultimate radiation from the reflector antenna is computed by simply integrating the usual untilted focal plane fields (which are feed-radiated fields ray traced onto the focal plane) using classic Fourier aperture theory [*Kildal*, 2000]. This method is applicable to all beam cases, being valid for axial beams, single off-axis beams, and multiple overlapping beams. These beam cases differ only in the excitation of the FPA feed and thus the fields arising on the untilted focal plane. It is asserted that the previously described integration of GO-ray projected fields over tilted apertures is solely for calculating the aperture subefficiencies (see following section) of off-axis beams and that it is not used for the computation of the far-field secondary radiation pattern of the reflector antenna.

2.3. Subefficiencies of the FPA-Fed Reflector

[19] The final but important branch of the overview presented here is the statement of the subefficiencies that are used as figures of merit to characterize the FPA-fed reflector, which are the ultimate quantities that have been computed and are presented in section 4. The total efficiency of the reflector system is expressed as

$$\varepsilon_{\text{tot}} = \varepsilon_{\text{ap}}\varepsilon_{\text{totrad}}, \tag{1}$$

where

$$\varepsilon_{\text{ap}} = \varepsilon_{\text{spill}}\varepsilon_{\text{illum}}\varepsilon_{\text{pol}}\varepsilon_{\text{phase}}\varepsilon_{\text{block}} \tag{2}$$

and

$$\varepsilon_{\text{totrad}} = \varepsilon_{\text{rad}}\varepsilon_{\text{decoup}}. \tag{3}$$

The aperture efficiency ε_{ap} comprises the usual spillover, illumination, polarization, phase, and blockage subefficiencies expressed by equation (2), whereas the total radiation efficiency $\varepsilon_{\text{totrad}}$ of equation (3) is composed of the conventional radiation efficiency ε_{rad} accounting for ohmic and dissipative losses as well as the decoupling efficiency $\varepsilon_{\text{decoup}}$ accounting for mutual coupling losses. Where ideal lossless materials are assumed, the radiation efficiency is unity, but generally not the decoupling efficiency of the array. In the present investigation, this ideal lossless condition is assumed, i.e., $\varepsilon_{\text{rad}} = 1$.

3. Embedded Element Analysis

[20] In spite of the preceding descriptive overview of the entire conceptual framework and computational procedures with references to published works of the author, the way to obtain the fields under the EES, although already implemented in the author's previous works, entails high levels of subtleties and has not yet been previously explained or reported. It is thus the purpose of this section to present for the first time

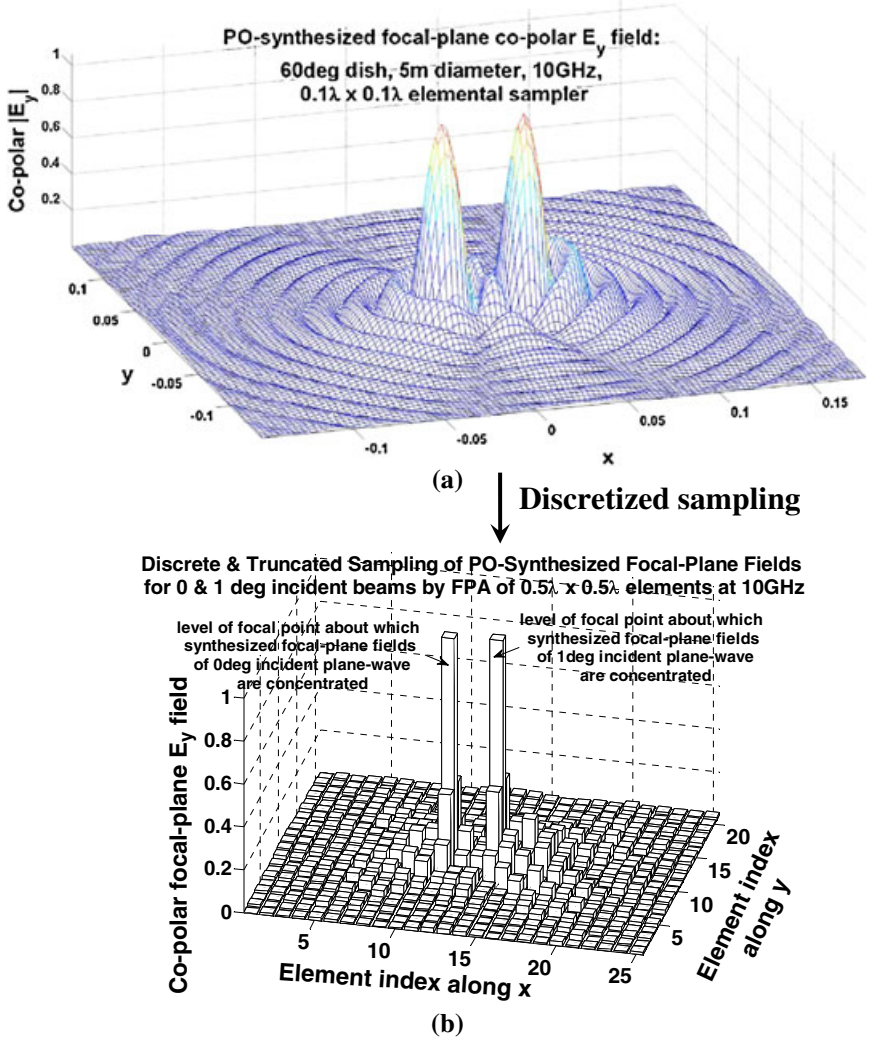

Figure 4. Synthesized focal plane fields by PO integration for overlapping 0° and 1° plane wave incidences onto the same 60° paraboloid at 10 GHz obtained by (complex value) addition of focal plane fields in Figures 3a and 3b, which show continuous and discretized amplitude levels (without phase information), respectively. Only the co-polar E_y field component is given and the xz plane of incidence considered.

the mathematical details of the underlying concepts behind the acquisition of the EES fields, which, as already emphasized earlier, constitutes an extremely fundamental and vital part of the analysis. Although the plain dielectric sheet cover is being investigated here, the case of a metallic patch array printed on a dielectric board and placed over the FPA, the configuration studied by *Ng Mou Kehn and Shafai* [2009], is considered and assumed in the analyses to follow, which would not at all affect the concepts to be relayed.

3.1. Fourier Transform and Mutual Coupling Concepts

[21] Let the spectral field (in k_x, k_y domain) radiated by the metallic patch into the region above the periodic patch array ($z > z_{i-1}$; see Figure 1) be stated as

$$\tilde{\vec{E}}^{ex}(k_x, k_y) = \sum_{p=1}^{N_p} a_p \tilde{\vec{f}}_p(k_x, k_y) \cdot \tilde{\tilde{G}}(k_x, k_y, z > z_{i-1}) \tag{4}$$

where a_p is the amplitude coefficient of the pth basis function expanding the patch electric current, with

$$\tilde{\vec{f}}_p(k_x, k_y) = \iint_{(x,y)\in \text{patch}} \underbrace{\vec{f}_p(x,y)}_{\substack{p\text{th basis function} \\ \text{of patch current}}} e^{j(k_x x + k_y y)} dx dy \tag{5}$$

being the two-dimensional (2D) Fourier transform of the pth basis electric current $\boldsymbol{f}_p(x, y)$ existing over the metallic patch parallel to the xy plane (one printed on the top surface of the dielectric slab within each unit cell; see Figure 1), and where $\tilde{\tilde{G}}(k_x, k_y, z > z_{i-1})$ is the spectral Green's function (numerical type, i.e., non-analytical) for multilayer structures, i.e., the G1DMULT routine.

[22] Subsequently, the spatial domain field is obtained through the inverse transform that involves only a summation over spectral components, i.e., discrete spectrum, due to the periodicity of the structure along x and y. This is expressed as follows:

$$\vec{E}^{ex}(x, y, z > z_{i-1}) = \frac{1}{d_x d_y} \sum_{m,n} \tilde{\vec{E}}^{ex}(k_x, k_y, z > z_{i-1}) e^{j k_{xm} x + k_{yn} y} \tag{6}$$

in which the discrete spectral coordinates are given by

$$k_{xm} = k_0 \sin\theta_0 \cos\phi_0 + 2m\pi/d_x, \quad k_{yn} = k_0 \sin\theta_0 \sin\phi_0 + 2n\pi/d_y$$

where m and n are integers; θ_0 and ϕ_0 are angular coordinates defining the direction of the dominant Floquet modal beam; d_x and d_y are the periods along x and y of the 2D periodic structure, respectively; and k_0 is the usual free space wave number. Under the phased array scenario, (θ_0, ϕ_0) defines the steered main beam direction.

[23] When all elements are excited for the phased array scenario beamed toward the direction defined by (k_{x0}, k_{y0}), the electric current over the (u, v)th patch centered at ($x = ud_x$, $y = vd_y$) is written as

$$\vec{J}^{(uv)\text{all}}\left(ud_x - \frac{d_x}{2} < x < ud_x + \frac{d_x}{2}, vd_y - \frac{d_y}{2} < y < vd_y + \frac{d_y}{2}\right) \quad (7)$$
$$= \sum_{p=1}^{N_p} a_p^{00(\text{all})} \overbrace{\vec{f}_p(x - ud_x, y - vd_y) e^{j k_{x0} u d_x + k_{y0} v d_y}}^{\rightarrow f_p^{uv}(x,y)}$$

which is valid only over the range of x and y values as explicitly indicated in the argument (the current is zero everywhere else). The spatial domain vector function $\boldsymbol{f}_p(x - ud_x, y - vd_y)$ represents the pth basis current of the (0, 0)th patch that is translated by ($x = ud_x$, $y = vd_y$) from the origin. The untranslated basis current ($u = v = 0$) is the generating basis current function for the periodic basis current function that spans throughout the entire array aperture. The variables k_{x0} and k_{y0} are the usual dominant Floquet harmonics pertaining to the steered main beam. The term $a_p^{00(\text{all})}$ is the solved amplitude coefficient for the (0, 0)th element under the phased array scenario steered to that particular main beam. The superscript "all" denotes the all-excited phased array scenario.

[24] Consequently, the current over the entire aperture $[-\infty < x < \infty, -\infty < y < \infty]$ can be expressed as a superposed sum of $\vec{J}^{(uv)\text{all}}$ in equation (7) over all u and v element indices, i.e.,

$$\vec{J}^{(-\infty<uv<\infty)\text{all}}_{\text{entire aperture}}(-\infty < x, y < \infty) \quad (8)$$
$$= \sum_{u,v=-\infty}^{\infty} \vec{J}^{(uv)\text{all}}\left(ud_x - \frac{d_x}{2} < x < ud_x + \frac{d_x}{2}, vd_y - \frac{d_y}{2} < y < vd_y + \frac{d_y}{2}\right)$$

[25] Now, let ζ_p^{uv} be the coefficient for the coupling from the (0, 0)th excited waveguide element in fundamental mode with index p_{in} (the only one excited) to the amplitude coefficient a_p^{uv} of the pth basis function of the (u, v)th patch current. Therefore, when only the (0, 0)th element is excited (the rest passively match terminated), the current over the (u, v)th patch can be written as

$$\vec{J}^{uv(\text{sole }00)}(x, y, z_{i-1}) = \sum_{p=1}^{N_p} \underbrace{A_{p_{in}}^{00} \zeta_p^{uv}}_{a_p^{uv(\text{sole})}} \vec{f}_p(x - ud_x, y - vd_y) \quad (9)$$

being the current over the (u, v)th patch when only the (0, 0)th element is excited, with all the rest passively match terminated.

[26] By inversing the definition of ζ_p^{uv}, let ζ_p^{-uv} be the coefficient for the coupling from the solely excited (u, v)th element in fundamental mode to the amplitude coefficient a_p^{00} of the pth basis function of the (0, 0)th patch current. Then, the reverse case of equation (9) is written as

$$\vec{J}^{00(\text{sole }uv)}\left(-\frac{d_x}{2} < x < \frac{d_x}{2}, -\frac{d_y}{2} < y < \frac{d_y}{2}, z_{i-1}\right)$$
$$= \sum_{p=1}^{N_p} \underbrace{A_{p_{in}}^{uv} \zeta_p^{-uv}}_{a_p^{00(\text{sole})}} \vec{f}_p(x, y) \in (0,0)\text{th patch} \quad (10)$$

being the current over the (0, 0)th patch when only the (u, v) th element is excited by the (p_{in})th mode. It is again asserted that this current function vanishes outside the range specified, i.e., outside the (0, 0)th patch.

[27] Therefore, superposing infinitely many (u, v)th cases of equation (10) to obtain the current over the (0, 0)th patch under the infinite phased array scenario when beamed toward a certain direction defined by (k_{x0}, k_{y0}), we have (with $A_{p_{in}}^{uv}$ set to unity for all u and v indices pertaining to a uniform phased array)

$$\vec{J}^{00(\text{all})}\left(-\frac{d_x}{2} < x < \frac{d_x}{2}, -\frac{d_y}{2} < y < \frac{d_y}{2}, z_{i-1}\right)$$
$$= \sum_{u,v=-\infty}^{\infty} \vec{J}^{00(\text{sole }uv)} \overbrace{e^{j k_{x0} u d_x + k_{y0} v d_y}}^{\substack{\text{for phase diff between} \\ (u,v)\text{th and} (0,0)\text{th}}}$$
$$= \sum_{u,v=-\infty}^{\infty} \sum_{p=1}^{N_p} \zeta_p^{-uv} \vec{f}_p(x, y) e^{j k_{x0} u d_x + k_{y0} v d_y} \quad (11)$$
$$= \sum_{p=1}^{N_p} \underbrace{\left[\sum_{u,v=-\infty}^{\infty} \zeta_p^{-uv} e^{j k_{x0} u d_x + k_{y0} v d_y}\right]}_{a_p^{00(\text{all})}} \vec{f}_p(x, y) = \sum_{p=1}^{N_p} a_p^{00(\text{all})} \vec{f}_p(x, y)$$

where $a_p^{00(\text{all})}$ is the amplitude coefficient of the pth basis function of the (0, 0)th patch current under the all-excited phased array scenario, which can also be inferred by setting $u = v = 0$ in equation (7). Note the very important exponential term that accounts for the phase shift between the (u, v)th element and the (0, 0)th element (at zero phase)—recall that in an infinite phased array scenario, the variation (of either fields or currents) of every element is the same in all elements, but with a phase difference determined by the phasing of the elements (phase gradient over the array) that determines the steered main beam direction. This pertains also to the dominant Floquet mode (k_{x0}, k_{y0}).

[28] Since this $a_p^{00(\text{all})}$ is scan dependent (under phased array scenario), let us write it as $a_p^{00(\text{all})}(\Phi_x = k_{x0} d_x, \Phi_y = k_{y0} d_y)$ with expressed argument. Explicitly stating this $a_p^{00(\text{all})}$ in equation (11),

$$a_p^{00(\text{all})}(\Phi_x, \Phi_y) = \sum_{u,v=-\infty}^{\infty} \zeta_p^{uv} e^{-j u \Phi_x + v \Phi_y} \quad (12)$$

where $\Phi_x = k_{x0} d_x$, $\Phi_y = k_{y0} d_y$.

[29] Therefore, the associated forward Fourier transform is

$$\zeta_p^{uv} = \frac{1}{4\pi^2} \int_{\Phi_x=-\pi}^{\pi} \int_{\Phi_y=-\pi}^{\pi} a_p^{00(\text{all})}\left(\Phi_x, \Phi_y\right) e^{j\,u\Phi_x + v\Phi_y} d\Phi_x d\Phi_y \tag{13}$$

[30] Placing this expression into equation (9), with $A_{p_{in}}^{00}$ in there set to unity (as we have considered uniformly excited phased array, with unit amplitude) and since the x and y coordinates are affected by neither the summation (over basis function index p) nor the integration (with respect to Φ_x and Φ_y), we are at liberty to arbitrarily define a new primed coordinate system with origin at ($x = ud_x$, $y = vd_y$), thus yielding the following:

$$\begin{aligned}&\overrightarrow{J}^{uv(\text{sole }00)}\left(-\frac{d_x}{2} < x' < \frac{d_x}{2}, -\frac{d_y}{2} < y' < \frac{d_y}{2}, z_{i-1}\right)\\ &= \frac{1}{4\pi^2}\sum_{p=1}^{N_p} \int_{\Phi_x=-\pi}^{\pi} \int_{\Phi_y=-\pi}^{\pi} a_p^{00(\text{all})}\left(\Phi_x, \Phi_y\right) e^{j\,u\Phi_x + v\Phi_y} d\Phi_x d\Phi_y \overrightarrow{f}_p\left(x', y'\right)\end{aligned} \tag{14}$$

where $\boldsymbol{f}_p(x', y')$ is the pth basis current of the (0, 0)th patch, being the generating basis current function of the entire periodic basis current function spanning over the whole array aperture.

[31] Upon using equation (7) in equation (14), we get

$$\begin{aligned}&\overrightarrow{J}^{uv(\text{sole }00)}\left(-\frac{d_x}{2} < x' < \frac{d_x}{2}, -\frac{d_y}{2} < y' < \frac{d_y}{2}, z_{i-1}\right)\\ &= \frac{1}{4\pi^2} \int_{\Phi_x=-\pi}^{\pi} \int_{\Phi_y=-\pi}^{\pi} \left\{ \begin{array}{l} \overrightarrow{J}^{(uv=00)\text{all}}\left(-\frac{d_x}{2} < x < \frac{d_x}{2}, -\frac{d_y}{2} < y < \frac{d_y}{2}, \Phi_x, \Phi_y\right) \\ \cdots \times e^{j\,u\Phi_x + v\Phi_y} d\Phi_x d\Phi_y \end{array} \right\}\end{aligned} \tag{15}$$

[32] Now, $\overrightarrow{J}^{(uv=00)\text{all}}$ has already been acquired via the solution of the infinite all-excited phased array problem (as described by *Ng Mou Kehn and Shafai* [2009]), and it is expressed as follows:

$$\overrightarrow{J}^{(uv=00)\text{all}} = \frac{1}{dxdy} \sum_{m,n} \sum_{p} a_p^{00(\text{all})}\left(\Phi_x, \Phi_y\right) \overrightarrow{\overrightarrow{f}}_p\left(k_{xm}, k_{yn}\right) e^{j\,k_{xm}x + k_{yn}y} \tag{16}$$

where $a_p^{00(\text{all})}$ is the solved amplitude coefficient of the pth RWG (after Rao, Wilton, and Glisson [*Rao et al.*, 1982]) basis function expanding the patch electric current, as was done by *Ng Mou Kehn and Shafai* [2009].

[33] Hence, with equation (16) placed into equation (15), we obtain

$$\begin{aligned}&\overrightarrow{J}^{uv(\text{sole }00)}\left(-\frac{d_x}{2} < x' < \frac{d_x}{2}, -\frac{d_y}{2} < y' < \frac{d_y}{2}, z_{i-1}\right) =\\ &= \frac{1}{4\pi^2 dxdy} \int_{\Phi_x=-\pi}^{\pi} \int_{\Phi_y=-\pi}^{\pi} \left\{ \left[\sum_{m,n} \sum_{p} a_p^{00(\text{all})}\left(\Phi_x, \Phi_y\right) \overrightarrow{\overrightarrow{f}}_p\left(k_{xm}, k_{yn}\right) e^{j\,k_{xm}x + k_{yn}y} \right] e^{j u\Phi_x + v\Phi_y} d\Phi_x d\Phi_y \right\}\end{aligned} \tag{17}$$

[34] Let us next write the far-zone electric field radiated by the patch current $\overrightarrow{J}_{\text{ap}}\left(x', y', z_{i-1}\right)$, under the EES, in which the primed x and y coordinates in the argument span over the entire aperture, as the following inverse transform:

$$\overrightarrow{E}_{\text{EES}}^{\text{far zone}}(x_o, y_o, z_o) = \frac{1}{4\pi^2} \int_{k_y=\infty}^{\infty} \int_{k_x=\infty}^{\infty} \underbrace{\overrightarrow{\overrightarrow{J}}_{\text{ap}}\left(k_x, k_y\right) \cdot \overrightarrow{\overrightarrow{G}}\left(k_x, k_y\right)}_{\overrightarrow{\overrightarrow{E}}\left(k_x, k_y, z_o\right)} e^{j\,k_x x_o + k_y y_o} dk_x dk_y \tag{18}$$

where

$$\overrightarrow{\overrightarrow{J}}_{\text{ap}}\left(k_x, k_y\right) = \int_{y'=-\infty}^{\infty} \int_{x'=-\infty}^{\infty} \overrightarrow{J}_{\text{ap}}\left(x', y'\right) e^{-j\,k_x x' + k_y y'} dx' dy' \tag{19}$$

with

$$\overrightarrow{J}_{\text{ap}}\left(x', y'\right) = \sum_{uv} \underbrace{\overrightarrow{J}^{uv(\text{sole})}\left(x', y'\right)}_{\text{of equation(9)}} e^{-j\,k_x u d_x + k_y v d_y} \tag{20}$$

in which the exponential term accounts for the phase shift from the (0, 0)th element with zero phase to the (u, v)th one, pertaining to a phase-steered beam direction corresponding to k_x and k_y.

[35] Placing equation (17) into equation (20), with an inconsequential change in the sign of the exponent for the inverse transform (discrete summation) adopting the more common convention, we have

$$\vec{J}_{\text{ap}}^{(k'_{x0},k'_{y0})}(x,y) = \frac{1}{4\pi^2 dxdy}\sum_{uv}\int_{\Phi_x=-\pi}^{\pi}\int_{\Phi_y=-\pi}^{\pi}\left\{\left[\sum_{m,n}\sum_{p} a_p^{00(\text{all})}(\Phi_x,\Phi_y)\vec{\tilde{\tilde{f}}}_p(k_{xm},k_{yn})e^{-j\,k_{xm}x+k_{yn}y}\right]e^{j\,u\Phi_x+v\Phi_y}d\Phi_x d\Phi_y e^{-j\,k'_{x0}ud_x+k'_{y0}vd_y}\right\} \tag{21}$$

where the primed k_{x0} and k_{y0} correspond to the observation direction under the EES.

[36] The k'_{x0} and k'_{y0} in the bracketed superscripts on the left sides of these two equations signify that these currents existing over the entire array aperture under the EES pertain to the situation where the field observation (under the EES) is toward that direction defined by these primed variables. Hence, there will be different current distributions over the entire array aperture for various field observation directions under the EES.

[37] Using the concept manifested by equation (21) and then denoting $\tilde{\tilde{G}}_{\text{patch}}^{F_w}$ as the spectral Green's function for the F_w field (F may be E or H, and w may be x, y, or z) radiated by spectral electric current excitation $\vec{\tilde{\tilde{f}}}_p(k_{xm},,k_{yn})$ (they are the pth basis functions of the patch electric currents), both under the multilayer scenario with the periodic patch array present, any general field component F_w can be expressed as

$$F_{w(k'_{x0},k'_{y0})}^{\text{EES}}(x,y,z) = \frac{1}{4\pi^2 dxdy}\sum_{uv}\sum_{m,n}\int_{\Phi_x=-\pi}^{\pi}\int_{\Phi_y=-\pi}^{\pi}\left\{\left[\sum_{p} a_p^{00(\text{all})}(\Phi_x,\Phi_y)\vec{\tilde{\tilde{f}}}_p(k_{xm},k_{yn})\cdot\tilde{\tilde{G}}_{\text{patch}}^{F_w}(k_{xm},k_{yn},z)\right]\right\}e^{-j\,k'_{x0}ud_x+k'_{y0}vd_y} \cdots \times e^{-j\,k_{xm}x+k_{yn}y}e^{j\,u\Phi_x+v\Phi_y}d\Phi_x d\Phi_y \tag{22}$$

where G denotes the spectral Green's function having its usual superscript notation for the field component involved and the subscript representing the kind and location of the source ("patch" here means electric current source over the PEC patch). The bracketed subscript on the left side containing k'_{x0} and k'_{y0} denotes that this field component under the EES pertains to the situation where the field observation (under the EES) is toward that direction defined by these primed variables.

[38] If we take the forward transform of equation (22), i.e., take $\int_{x'=-\infty\to-\frac{d_x}{2}}^{\infty\to\frac{d_x}{2}}\int_{y'=-\infty\to-\frac{d_y}{2}}^{\infty\to\frac{d_y}{2}}\text{—}\cdot e^{j(k'_{x0}x'+k'_{y0}y')}dx'dy'$ throughout, we obtain

$$F_w^{\text{EES}}(k'_{x0},k'_{y0}) = \frac{1}{4\pi^2 d_x d_y}\sum_{uv}\int_{y'=-\frac{d_y}{2}}^{\frac{d_y}{2}}\int_{x'=-\frac{d_x}{2}}^{\frac{d_x}{2}}\left\{\sum_{m,n}\sum_{p}\int_{\Phi_y=-\pi}^{\pi}\int_{\Phi_x=-\pi}^{\pi}\Omega(\Phi_x,\Phi_y)e^{-j\,k_{xm}x+k_{yn}y}e^{j\left[u\Phi_x+v\Phi_y\right]}d\Phi_x d\Phi_y\right\}\cdots \cdots\times e^{-j\left[uk'_{x0}d_x+v\,k'_{y0}d_y\right]}e^{+j\,k'_{x0}x'+k'_{y0}y'}dx'dy' \tag{23}$$

in which Ω has been introduced to represent

$$\Omega(\Phi_x,\Phi_y) = \Omega_x(\Phi_x)\Omega_y(\Phi_y) = \sum_{p} a_p^{00(\text{all})}(\Phi_x,\Phi_y)\vec{\tilde{\tilde{f}}}_p(k_{xm},k_{yn})\cdot\tilde{\tilde{G}}_{\text{patch}}^{F_w}(k_{xm},k_{yn},z), \tag{24}$$

which is a quantity that is scan dependent, i.e., varies as a function of θ and ϕ via $k_{x0}=k_0\sin\theta\cos\phi=2\pi f\sqrt{\mu_0\varepsilon_0}\sin\theta\cos\phi$ and $k_{y0}=k_0\sin\theta\sin\phi=2\pi f\sqrt{\mu_0\varepsilon_0}\sin\theta\sin\phi$. The dependence on $\Phi_x=k_{x0}d_x$ and $\Phi_y=k_{y0}d_y$ is assumed separable, as shown.

[39] Note the reduction of surface integration limits to cover only the unit cell $-\frac{d_x}{2}\le x'\le\frac{d_x}{2}$; $-\frac{d_y}{2}\le y'\le\frac{d_y}{2}$ of the (uv) th element. Also, observe the incorporation of primes to the k_{x0} and k_{y0} quantities lying outside the integration with respect to $\Phi_x=k_{x0}d_x$ and $\Phi_y=k_{y0}d_y$ so as to distinguish them from the integration variables (unprimed). With further rearrangement, swapping prime and unprimed coordinates, and applying the well-known identity, we have

$$\sum_{r=-\infty}^{\infty}e^{jr\,\psi-\psi'} = \begin{cases}2\pi \text{ when } \psi=\psi'\\ 0 \text{ otherwise}\end{cases} = 2\pi\delta(\psi-\psi')$$

describing both $1\rightleftharpoons\delta$ and the shifting properties of the Fourier transform. With further use of another well-known result,

$$\int_{w=-\frac{c}{2}}^{\frac{c}{2}} e^{j\frac{2p\pi}{d_w}w}dw = c\delta_{p0} = \begin{cases} c \text{ when } p=0 \\ 0 \text{ otherwise} \end{cases}$$

and using equation (24) for $m=n=0$, we obtain the following:

$$\begin{aligned}
&\widetilde{\widetilde{F}}_w^{\mathrm{EES}}(k_x,k_y;z) \\
&= \frac{1}{d_x d_y}\sum_p a_p^{00(\mathrm{all})}(\Phi_x = k_x d_x, \Phi_y = k_y d_y)\,\widetilde{\widetilde{\vec{f}}}_p(k_x,k_y)\cdot\widetilde{\widetilde{G}}_{\mathrm{patch}}^{F_w}(k_x,k_y z) + \cdots \\
&\cdots + \frac{1}{d_x d_y}\sum_{pqr} A_{pqr}^{00(\mathrm{all})}(\Phi_x = k_x d_x, \Phi_y = k_y d_y)\,\widetilde{\widetilde{\vec{g}}}_{pqr}(k_x,k_y)\cdot\widetilde{\widetilde{G}}_{apert}^{F_w}(k_x,k_y z)
\end{aligned} \tag{25}$$

[40] Hence, the strength of the F_w field component of the dominant (0, 0)th Floquet modal plane wave (where main beam is "mb") of the infinite phased array pertaining to a certain $(k_x, , k_y) = (k_{x0}, , k_{y0}) = \left(k_x^{\mathrm{mb}}, k_y^{\mathrm{mb}}\right) = (k_0 \sin\theta_{\mathrm{mb}} \cos\phi_{\mathrm{mb}}, k_0 \sin\theta_{\mathrm{mb}} \sin\phi_{\mathrm{mb}})$ is also the Fourier-transformed spectral domain field component $\widetilde{\widetilde{F}}_w(k_x,k_y)$ under the EES, being the amplitude of the (k_x, k_y)th spectral plane wave component. It is equation (25) that is the ultimately computed quantity used in equations (30) and (31) for the radiated fields under the EES.

3.2. Embedded Element Radiation

[41] Referring to the work of *Sipus* [1997] on far-field calculations using PEC equivalence involving equivalent magnetic current source aperture, we write the following PEC equivalent magnetic current located at $z=z_{ap}$ just above the PEC patch array (see Figure 1):

$$\vec{M}_{\mathrm{eq}}^{\mathrm{EES}}(x',y',z'=z_{\mathrm{ap}}) = \vec{E}^{\mathrm{EES}}(x',y',z'=z_{\mathrm{ap}}) \times \hat{z} \tag{26}$$

$$= \hat{x}\underbrace{E_{y(k'_{x0},k'_{y0})}^{\mathrm{EES}}(x',y',z'=z_{\mathrm{ap}})}_{\text{of equation(22)}} + \hat{y}\left[\underbrace{-E_{x(k'_{x0},k'_{y0})}^{\mathrm{EES}}(x',y',z'=z_{\mathrm{ap}})}_{\text{of equation(22)}}\right]$$

[42] The electric field components on the right side are those of equation (22). From the work of *Sipus* [1997], the far field is

$$\vec{E}_{\mathrm{far}}^{\mathrm{EES}}(r,\theta,\phi) = -2\frac{jke^{-jkr}}{4\pi r}\int_{y'=-\infty}^{\infty}\int_{x'=-\infty}^{\infty} [\vec{M}_{\mathrm{eq}}^{\mathrm{EES}}(x',y'z_{\mathrm{ap}}) \times \hat{r}(\theta,\phi)]e^{j\,k_x x' + k_y y' + k_z z_{\mathrm{ap}}}dx'\,dy' \tag{27}$$

where the factor 2 at the front is due to imaging. The integration spans over the entire source aperture located at $z=z_{\mathrm{ap}}$ with infinite extent along the transverse x-y plane. The wave numbers are

$$k_x = k\sin\theta\cos\phi; k_y = k\sin\theta\sin\phi; k_z = k\cos\theta \tag{28}$$

where (θ, ϕ) are the angular coordinates of the observation direction under the EES.

[43] Placing equation (26) in equation (27),

$$\vec{E}_{\mathrm{far}}^{\mathrm{EES}}(r,\theta,\phi) = -\frac{jke^{-jkr}}{2\pi r}e^{jk_z z_{\mathrm{ap}}}\int_{y'=-\infty}^{\infty}\int_{x'=-\infty}^{\infty}\begin{pmatrix} E_y^{\mathrm{EES}} \\ -E_x^{\mathrm{EES}} \\ 0 \end{pmatrix} \times \begin{pmatrix} \sin\theta\cos\phi \\ \sin\theta\sin\phi \\ \cos\theta \end{pmatrix} e^{j\,k_x x' + k_y y'}\,dx'\,dy' \tag{29}$$

[44] Using $\hat{\theta} = \hat{x}\cos\theta\cos\phi + \hat{y}\cos\theta\sin\phi - \hat{z}\sin\theta$ and $\hat{\phi} = -\hat{x}\sin\phi + \hat{y}\cos\phi$, the θ and ϕ components of this far-zone electric field under the EES can be expressed separately as follows:

$$\begin{aligned}
E_\theta^{\mathrm{EES}}(r,\theta,\phi) &= \frac{e^{-jkr}}{r}G_\theta^{\mathrm{EES}}(\theta,\phi) \\
&= \frac{jke^{-jkr}}{2\pi r}e^{jk_z z_{\mathrm{ap}}}\left[\underbrace{\widetilde{\widetilde{E}}_x^{\mathrm{EES}}(k_x,k_y,z_{\mathrm{ap}})}_{\text{of equation(25)}}\cos\phi + \underbrace{\widetilde{\widetilde{E}}_y^{\mathrm{EES}}(k_x,k_y,z_{\mathrm{ap}})}_{\text{of equation(25)}}\sin\phi\right]
\end{aligned} \tag{30}$$

$$\begin{aligned}
&E_\phi^{\mathrm{EES}}(r,\theta,\phi) \\
&= \frac{e^{-jkr}}{r}G_\phi^{\mathrm{EES}}(\theta,\phi) = -\frac{jke^{-jkr}}{2\pi r}e^{jk_z z_{\mathrm{ap}}} \\
&\left[\underbrace{\widetilde{\widetilde{E}}_x^{\mathrm{EES}}(k_x,k_y,z_{\mathrm{ap}})}_{\text{of equation(25)}}\cos\theta\sin\phi - \underbrace{\widetilde{\widetilde{E}}_y^{\mathrm{EES}}(k_x,k_y,z_{\mathrm{ap}})}_{\text{of equation(25)}}\cos\theta\cos\phi\right]
\end{aligned} \tag{31}$$

in which the $\widetilde{\widetilde{E}}_w^{\mathrm{EES}}(k_x,k_y,z_{\mathrm{ap}})$ (w is x or y) is from equation (25).

[45] Hence, the essence here is that any certain far-field observation direction (θ, ϕ) under the EES determines a certain spectral component (k_x, k_y) [defined in equation (28)] of the aperture electric field (related to the PEC equivalent magnetic current source sheet), also under the EES. As asserted earlier, just after equation (25), this spectral (k_x, k_y) component of the E field (say, the E_w component) under the EES is simply the strength of that E_w field component of the dominant (0, 0)th Floquet modal plane wave (main beam) of the infinite phased array that is steered toward a certain main beam direction $(\theta_{\mathrm{mb}}, \phi_{\mathrm{mb}})$, with $(k_x, k_y) = (k_{x0}, k_{y0}) = \left(k_x^{\mathrm{mb}}, k_y^{\mathrm{mb}}\right) = (k_0 \sin\theta_{\mathrm{mb}} \cos\phi_{\mathrm{mb}}, k_0 \sin\theta_{\mathrm{mb}} \sin\phi_{\mathrm{mb}})$.

[46] Subsequently, by basic Poynting's power theorem, the total power radiated out into the half-space above the periodic patch array under the EES is

$$P^{\mathrm{EES}} = \frac{1}{2\eta}\int_{\phi=0}^{2\pi}\int_{\theta=0}^{\pi/2}\left|G_{\theta}^{\mathrm{EES}}(\theta,\phi)\right|^2 + \left|G_{\phi}^{\mathrm{EES}}(\theta,\phi)\right|^2 \sin\theta d\theta d\phi \quad (32)$$

where $\eta = \sqrt{\mu/\varepsilon}$ is the well-known intrinsic wave impedance of the medium above the array (typically vacuum).

4. Numerical Results and Discussion

[47] All numerical results presented herein for the dielectric-covered HRW array were generated by the moment method code developed according to the analysis and formulation just described. The computed data for HRW arrays without any form of cover were also obtained by the code constructed by *Ng Mou Kehn and Kildal* [2005].

4.1. Universal Conditions

[48] The fixed conditions that apply throughout the numerical investigations are first declared. A constant frequency of 10 GHz is considered and a square unit cell is studied, for which the periods d_x and d_y along x and y, respectively, are both equal to half a wavelength, i.e., 15 mm. The dimensions along x and y of the likewise square elemental waveguide aperture are $l_x = 0.98d_x = l_y = 0.98d_y$.

[49] The 10 GHz frequency is also the TEM frequency of the HRW elements. Hence, the waveguides are operated at the hard condition [*Ng Mou Kehn and Kildal*, 2005]. The ratio of the side slab thickness (any of the two slabs) to the total waveguide width is maintained at 1:40 throughout. In this way, the linearly polarized aperture fields over the dominant central air region are uniform in amplitude, thus providing "clean" elemental samplers of the focal plane fields.

[50] A subarray population of 21×21 is used in the sampling of the focal plane fields corresponding to the various beam angles. As explained in section 2.2.1, these focal plane fields are synthesized by integration of the PO currents arising on the paraboloid surface, which are induced by the incident plane waves (on receive) along the respective beam directions (on transmit). In the present study, a paraboloidal reflector with a half-subtended (dish) angle of 60° and a diameter of 5 m is considered. An additional tier of "dummy" (unexcited) elements comprising a four-element-thick track surrounding the periphery of the square excited portion (21×21) of the array is included in the analysis. By taking the coupled powers (especially from the excited edge elements) lost into these dummy boundary elements into account, the accuracy in the behavior of the excited elements near the edge of the subarray is improved. Hence, the total number of elements that are actually calculated, including both excited and non-excited ones, is 29×29.

[51] For off-axis beams, the synthesized sets of concentric focal plane field rings are displaced from the focal point of the paraboloid. In the present study, the geometric centers

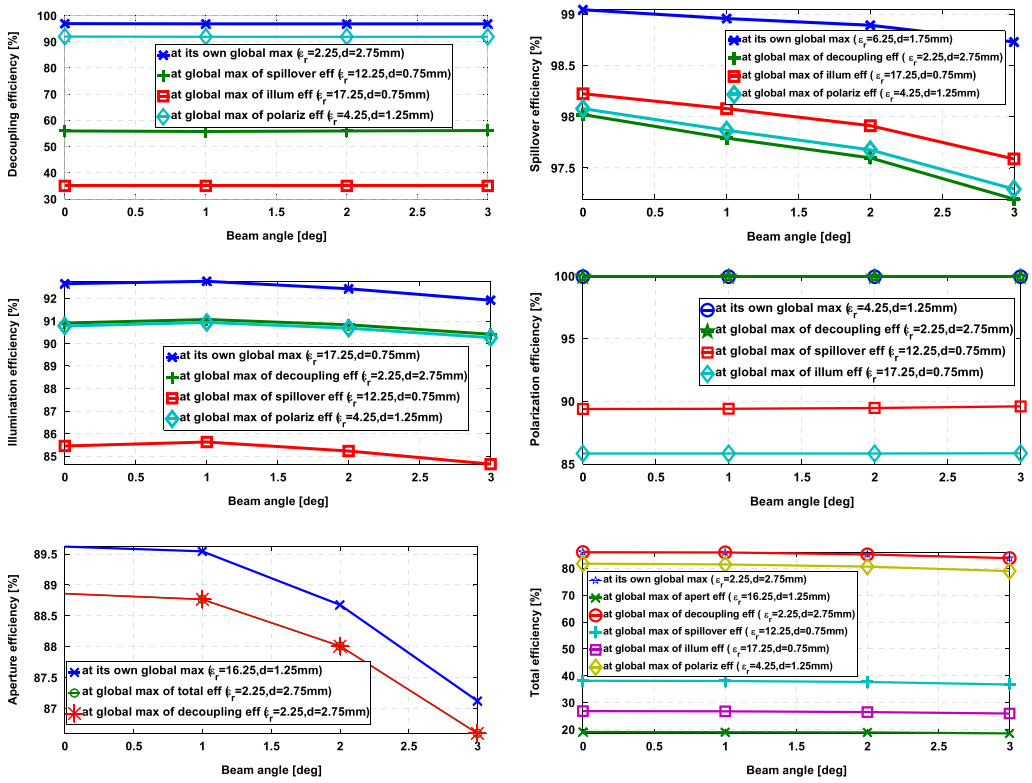

Figure 5. Each subplot gives the variation of a certain subefficiency (or total efficiency for the last one) with beam angle at various (ε_r, d) slab cases corresponding to its own global maximum as well as the global maxima of the other subefficiencies. This figure is for the 60° half-subtended angle of a parabolic reflector.

of the 21 × 21 FPA feeds and those of the various sets of displaced focal plane field rings (corresponding to different beams) are always made to coincide.

4.2. Dielectric-Covered Versus Uncovered FPAs

[52] The parameters of the dielectric layer investigated here are relative permittivity and thickness (ε_r and d, respectively, in Figure 1). Two categories of results are presented separately, one for single scanned beams and another for simultaneously overlapping beams. For the latter category, two beams are considered in this work.

4.2.1. Single Scanned Beam

[53] An optimization was conducted over the two aforementioned dielectric sheet parameters (ε_r and d) on the computed subefficiencies of the 60° paraboloid with a 5 m diameter fed by an HRW FPA covered with dielectric sheets having those attributes within the parametric search space for various beam angles ($\alpha = 0°$, 1°, 2°, and 3°). Each subplot in Figure 5 gives the variation of a certain subefficiency (ε_{decoup}, ε_{spill}, ε_{illum}, ε_{pol}, or ε_{ap}) as well as the total efficiency ε_{tot} (the last subplot) with beam angle, with each trace pertaining to a certain (ε_r, d) slab case corresponding to either its own optimal value or that associated with the maximum of any of the other three subefficiencies. Findings from this optimization interestingly reveal that, with the sole exception of the phase subefficiency, when a certain subefficiency is globally maximum under a certain slab configuration (ε_r, d) for a particular beam angle, it is also optimal with that same dielectric sheet for all other considered beam angles, as the legends in all subplots in Figure 5 show. Particularly, for the total efficiency [equation (1)] in the last subplot, being the ultimate performance indicator, there is an optimum slab configuration of ($\varepsilon_r = 2.25$, $d = 2.75$ mm) that is universal to all investigated beam angles. In addition, most intriguingly, this optimum dielectric cover coincides with that of the decoupling efficiency ε_{decoup} [of equation (3)], as evidenced by the last two subplots in Figure 5. This indicates the intimate connection between the overall performance and the decoupling efficiency (more on

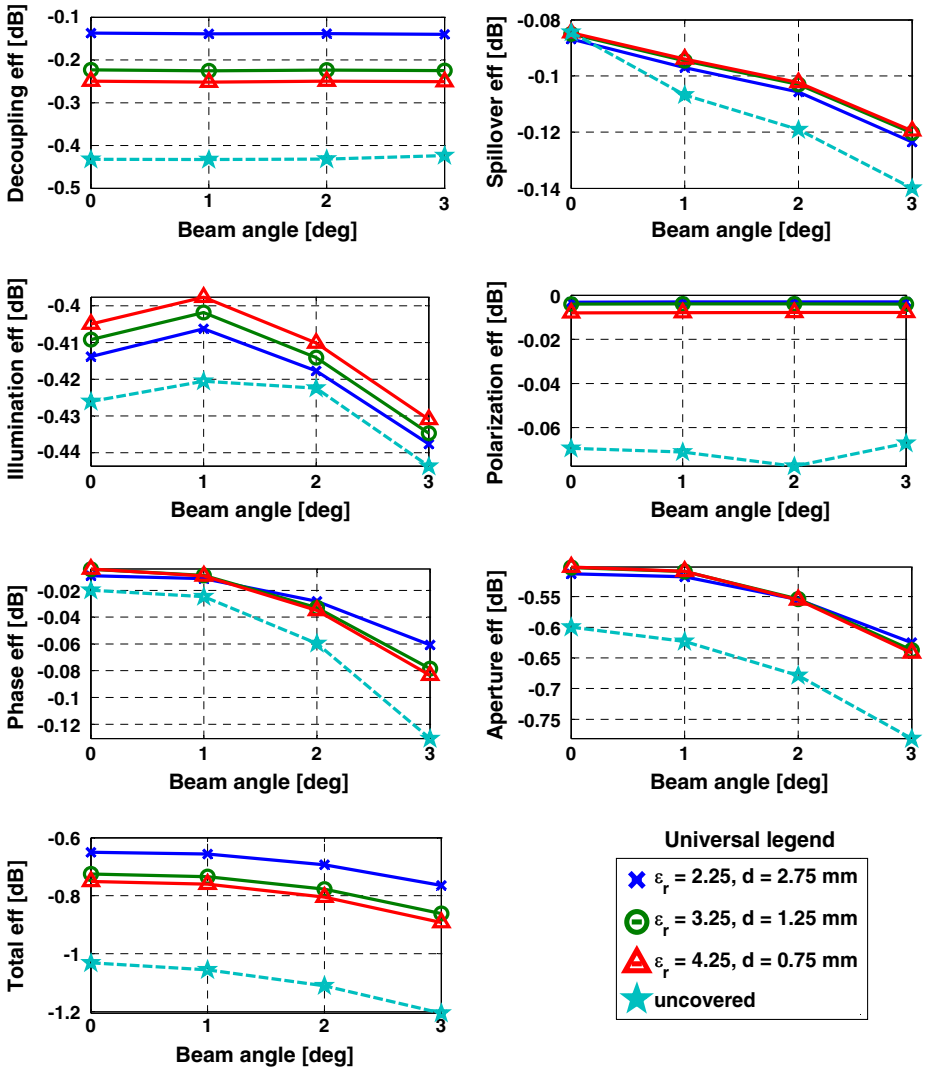

Figure 6. (a) Variation of subefficiencies with beam angle for a dielectric-covered 21 × 21 HRW FPA for the three best (ε_r, d) combination pairs. (b) Improvement of subefficiencies by the three best slab-covered FPAs as compared to uncovered FPAs for a range of beam angles. (c) Fractional degradation of subefficiencies with respect to axial level.

this later). By mere inspection of the plots for the decoupling and polarization subefficiencies (ε_{decoup} and ε_{pol}), it is readily observed that the use of dielectric sheets taking on the (ε_r, d) configuration pertaining to the maximum value of either the spillover subefficiency or the illumination subefficiency results in a drastic fall in both ε_{decoup} and ε_{pol}. As for the illumination subefficiency, it is also easily seen that it suffers severe degradation when the slab cover assumes the (ε_r, d) configuration of the maximum spillover subefficiency. Only the spillover subefficiency is not adversely affected by a dielectric layer associated with the maximum illumination subefficiency, although this is inconsequential, since as long as a slab cover exacerbates just any single subefficiency, it compromises the entire overall performance (total efficiency). Therefore, under no circumstance should the dielectric sheet take on the (ε_r, d) configuration of the maximum spillover or illumination subefficiency.

[54] On the contrary, operating under slab conditions corresponding to the maximum values of either the decoupling subefficiency or the polarization subefficiency does not give rise to an overly detrimental performance of any of the other three remaining subefficiencies. This is even in spite of the fact that the spillover subefficiency instead sustains the two strongest declinations from its maximum value when the slab cover takes on (ε_r, d) conditions linked with the maximum decoupling and polarization subefficiencies, simply because this loss in spillover efficiency is only by amounts within just 2% (see the narrow vertical axis range of the spillover efficiency plot), thus not having any significant impact. An interesting observation is that the beneficial

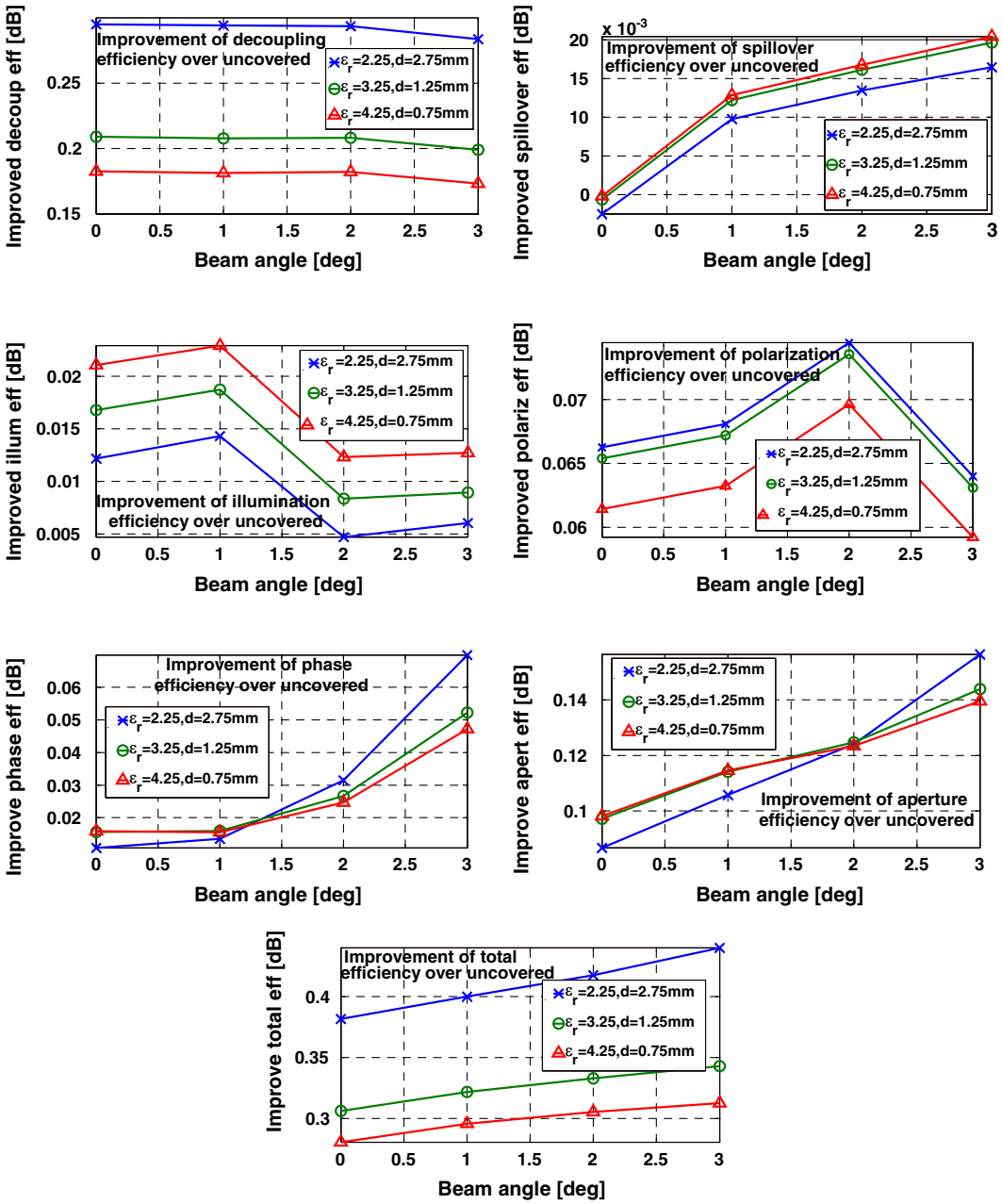

Figure 6. (Continued)

effects of operating under slab conditions pertaining to the maximum decoupling and polarization subefficiencies are rather similar, in that they both give rise to comparably high performance levels of all subefficiencies, not only for the other two subefficiencies (spillover and illumination) but also for the one (decoupling or polarization) other than themselves. But even so, the decoupling efficiency is still found to emerge as the more pertinent of the two, wielding a stronger influence than the polarization efficiency, thereby being the ultimate solitary factor that vitally dictates the overall efficiency performance of the parabolic reflector fed by an HRW FPA covered with a dielectric sheet. This is better appreciated by the last subplot in Figure 5 for the total efficiency as the vertical axis quantity, in which the fact that the decoupling efficiency is still superior to the polarization efficiency in promoting the total efficiency is evident. Employing a dielectric slab for optimal polarization efficiency is still inferior to using one for maximum decoupling efficiency, which (the latter slab) in fact shares exactly the same set of sheet parameters ($\varepsilon_r = 2.25$, $d = 2.75$ mm) with the optimum total efficiency. Operating under slab conditions for optimum polarization efficiency nonetheless yields the second best performance, as conveyed by the last subplot in Figure 5 for the total efficiency. The devastating effects of using dielectric covers in connection with the highest spillover or illumination subefficiency on the overall performance are also clear from Figure 5, just as what had been discussed. At this juncture, we can loop back to the statement made earlier about the close ties of the decoupling efficiency with the total efficiency. The decoupling efficiency is thus singularly responsible for the general performance of the dielectric-covered HRW FPA-fed reflector, and maximizing it translates to the optimal overall health of the antenna system.

[55] Singling out the best performing case of ($\varepsilon_r = 2.25$, $d = 2.75$ mm) and two other closely competing ones, namely, ($\varepsilon_r = 3.25$, $d = 1.25$ mm) and ($\varepsilon_r = 4.25$, $d = 0.75$ mm), the comparisons of their various subefficiencies with those of their uncovered counterparts are given in Figure 6a. As can be clearly seen, these best dielectric slab performers all provide overall efficiencies that are superior to those of the uncovered FPAs, for all beam angles. This constitutes an important finding: when a dielectric layer improves the performance of a certain beam angle, it also does so for all other beam angles. This elevates the advantages and desirability of such FPA covers. For near-axial beams (small beam angles), the optimal dielectric cover raises the total efficiency of the uncovered FPA by around 0.3 dB, but even more (beyond 0.4 dB enhancement) for larger beam angles (3° in our case; see Figure 6b). Therefore, we have demonstrated the ability of dielectric covers to improve the overall efficiency of FPA-fed reflectors, not only for one beam but over a range of beam angles, and their advantage over uncovered FPAs becomes stronger with off-axis scanning.

[56] The differential performance with beam angle is now presented. Figure 6b conveys the improvement of all subefficiencies by the three best performing slab-covered FPAs over their uncovered counterparts, being simply the difference in decibel levels in Figure 6a. As can be seen, depending on which subefficiency is being considered, the aforementioned order of ($\varepsilon_r = 2.25$, $d = 2.75$ mm), ($\varepsilon_r = 3.25$, $d = 1.25$ mm), and ($\varepsilon_r = 4.25$, $d = 0.75$ mm) could be in either descending order or ascending order of performance. It is however the total efficiency that ultimately matters, which cannot be deduced from looking at just one or even a few subefficiencies. Instead, all subefficiencies contributing to the overall performance of the FPA-fed reflector system must be taken into account, as has been done here. As asserted earlier, the decoupling efficiency is found to play the primary role in dictating the optimal slab, thus highlighting its utmost importance. Focusing on the last subplot in Figure 6b on the total efficiency, it is evident that the benefit of all dielectric covers becomes intensified as the beam angle increases (seen by the positive sloping), with the best cover ($\varepsilon_r = 2.25$, $d = 2.75$ mm) providing the greatest advantage, attaining an impressive 0.44 dB or 11% enhancement upon the 3° beam.

[57] The fractional degradation of the various subefficiencies with respect to the level of each respective axial beam due to

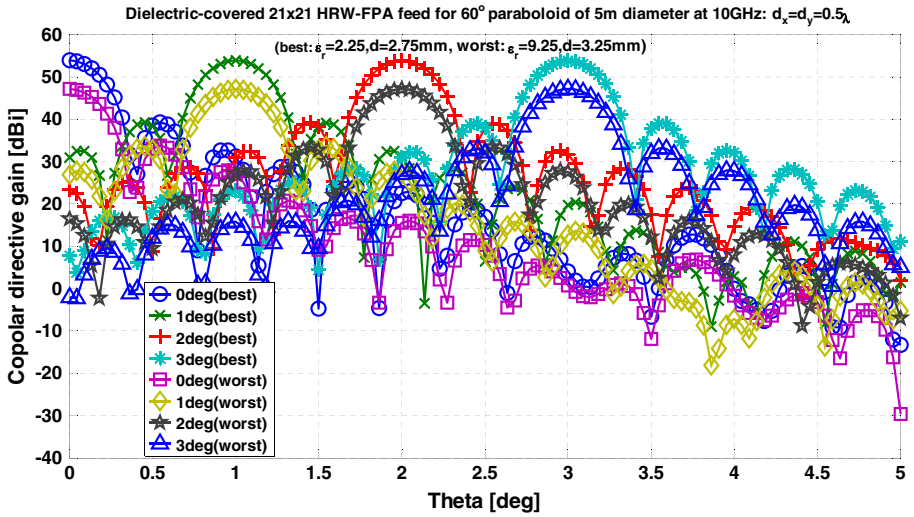

Figure 7. Directive gain patterns of 60° paraboloid (5 m diameter) fed by the best ($\varepsilon_r = 2.25$, $d = 2.75$ mm) and worst ($\varepsilon_r = 9.25$, $d = 3.25$ mm) performing dielectric covers placed over a 21×21 FPA comprising $d_x = d_y = \lambda/2$ elements at 10 GHz for various beam angles (0°, 1°, 2°, and 3°). The difference in directivity (toward beamed angle) between the best and worst performers equals the difference in their total efficiency.

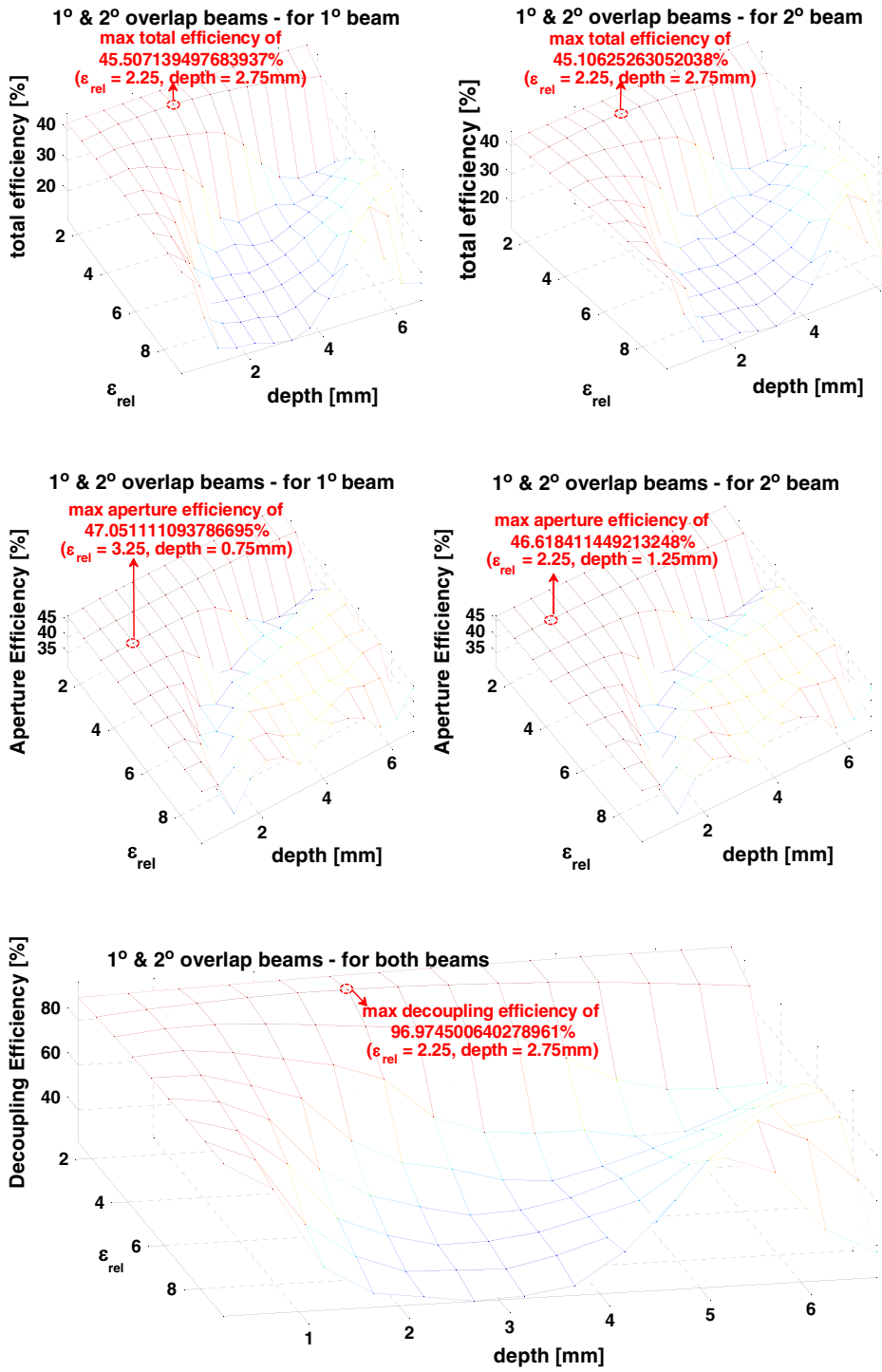

Figure 8. (a) Total efficiency plotted against relative permittivity ε_r and depth d of the dielectric sheet for overlapping beam angles $\alpha = 1°$ and 2°; left: 1° beam, right: 2° beam. The global maxima of 45.5071395% and 45.1062526% correspond to the 1° and 2° beams, respectively, both at ($\varepsilon_r = 2.25$, $d = 2.75$ mm). (b) Aperture efficiency plotted against relative permittivity ε_r and depth d of the dielectric sheet for overlapping beam angles $\alpha = 1°$ and 2°; left: 1° beam, right: 2° beam. The global maxima of 47.051111093786695% and 46.618411449213248% at ($\varepsilon_r = 3.25$, $d = 0.75$ mm) and ($\varepsilon_r = 2.25$, $d = 1.25$ mm) are for the 1° and 2° beams, respectively. (c) Decoupling efficiency plotted against relative permittivity ε_r and depth d of the dielectric sheet for overlapping beam angles $\alpha = 1°$ and 2° (pertaining to both beams). The global maximum of 96.9745% at ($\varepsilon_r = 2.25$, $d = 2.75$ mm) coincides with that of the total efficiency as well as the total and decoupling efficiencies of all other investigated beam pair angles.

beam scanning is provided in Figure 6c. Like before, whether the uncovered FPA or slab-covered version performs better depends on which subefficiency is looked at. For the total efficiency, it is found that all dielectric-covered FPAs sustain less relative losses than their uncovered versions as the beam angle increases. The best slab ($\varepsilon_r = 2.25$, $d = 2.75$ mm) again offers the least deterioration, falling to only -0.115 dB or 97.4% of the axial beam efficiency upon the 3° beam as opposed to the -0.174 dB or 96.1% drop suffered by the uncovered FPA. In other words, the sheath "slows down" the degradation with increasing beam obliquity as compared to the case without it. Hence, the dielectric-covered configuration is not only better than its unshielded counterpart for every beam angle but also superior in terms of deterioration rate with the beam angle. All these studies thus show that when an optimal dielectric cover is found, it also performs the best in terms of differential performance, which is an excellent aspect.

[58] The co-polar directive gain plots of the parabolic reflector fed by the best ($\varepsilon_r = 2.25$, $d = 2.75$ mm) and among the poorer ($\varepsilon_r = 9.25$, $d = 3.25$ mm) performing dielectric covers for the four beam angles (0°, 1°, 2°, and 3°) are presented in Figure 7. These secondary field patterns are generated by Fourier integration of the aperture fields obtained via GO projection of the primary FPA feed–radiated fields. It is noted that the Fourier integrations are performed over the usual untilted focal plane aperture (perpendicular to the reflector axis), even for off-axis beams (the tilted elliptical aperture concept described in section 2.2.2.2 is only for the calculation of the subefficiencies). These patterns are computed in the azimuthal plane containing the steered beams ($\phi = 0$ here). As clearly seen from these radiation patterns, the various main lobes are reproduced very accurately toward the respective beam angles. The main beam levels of the best slab performer are all close to (just less than 1 dB below) the 54.4 dBi theoretical maximum directivity (for the present 167λ meter paraboloidal diameter), in view of the high total aperture efficiencies, all about -0.65 to -0.75 dB, both also being less than 1 dB (see the best performer in Figure 6a). On the other hand, the weakly performing dielectric cover selected for comparison gives main beam gain levels of around 47 dBi, being 7.4 dB below the theoretical maximum. This concurs well with its approximate -7.25 dB ($\approx$19%) total efficiency for all four beam angles [for this ($\varepsilon_r = 9.25$, $d = 3.25$ mm)]. This aspect accentuates the remarkable correctness and thus astounding beauty of the entire theoretical framework laid out in sections 2 and 3 from which these computed results are generated—that the efficiencies computed by field integration of the focal planes [tilted (oblique beams) or untilted (axial beams)] and by calculation of the FPA feed–radiated powers would be so profoundly coherent with the secondary radiation pattern of the reflector generated by Fourier aperture integration of the (untilted) focal plane fields, a phenomenon that is certainly difficult to achieve without immense integrity of the formulated theories and concepts. This result exemplifies how vital it is to include the decoupling efficiency for complete and accurate characterization of the total antenna system, as we have aptly done here. Because had it been otherwise, e.g., only the conventional aperture subefficiencies of reflectors were considered, an incorrect quantification of the performance would result, showing up as discrepancies in drop levels in the radiation patterns of the reflector.

4.2.2. Overlapping Dual Beams

[59] We have shown that dielectric covers placed over FPA feeds of parabolic reflectors are able to enhance the total efficiency of single steered beams. We now proceed to explore the prospects of such layers in improving the performance of simultaneously overlapping multiple beams as well. A similar optimization procedure was performed on the various subefficiencies and the total efficiency of various pairs of overlapping beams over ε_r and d. As explained in section 2.2.3, each beam of every pair has its own total efficiency and separate set of subefficiencies, except for the decoupling and spillover efficiencies that are shared by both beams. Here the same 60° paraboloid with a 5 m diameter is fed by dielectric-covered FPAs excited (in a truncated and discretized manner) according to the superposed focal plane fields synthesized from the respective pair of incident plane waves associated with the two beam directions, as explained in section 2.2.3. The various beam pairs investigated are permutations of 0°, 1°, 2°, and 3°, hence a total of six cases. Figures 8a, 8b, and 8c give the contour plots of the total, aperture, and decoupling efficiencies, respectively, versus the relative permittivity ε_r and depth d of the dielectric cover, for the 1° and 2° beam pair, just as the selected case for illustration. In each of the former two figures, the subplots to the left and right are, respectively, for the 1° and 2° beams. The optimal efficiency value is also indicated along with its associated slab conditions (ε_r, d) in each contour plot. The results for the other five beam pair cases, namely, 0° and 1°, 0° and 2°, 0° and 3°, 1° and 3°, as well as 2° and 3°, are not presented due to space limitation and because they look similar from the perspective of the contour plots. Textually describing the results, it has been found that for any beam pair, the maximum total efficiencies of both beams interestingly occur at the same optimum dielectric cover ($\varepsilon_r = 2.25$, d = 2.75 mm). Amazingly, all investigated pairs of overlapping dual beams share that same common optimum dielectric sheet, being $\varepsilon_r = 2.25$ and $d = 2.75$ mm, that produces the maximum total efficiency for both beams of every pair. More fascinatingly, this optimal slab configuration is exactly the same as that of all solitary beams considered in section 4.2.2. In addition, just as is the case for single steered beams, the slab conditions pertaining to optimum decoupling efficiencies for all beam pairs are exactly the same as those that yield the optimal total efficiencies for both beams of the pair—in the same way as how the decoupling efficiency plays the predominant role in dictating the combined performance for solitary beams. This again elucidates the momentous

Table 1. Aperture and Total Efficiencies of Various Pairs of Overlapping Beams for Uncovered FPA Feed for Dual-Beam Reflectors

α	ε_{ap} (dB)		ε_{tot} (dB)	
0° and 1°	−3.465	−3.455	−3.913	−3.903
0° and 2°	−3.813	−3.900	−4.207	−4.294
0° and 3°	−3.635	−3.905	−4.067	−4.336
1° and 2°	−3.495	−3.515	−3.941	−3.961
1° and 3°	−3.847	−3.976	−4.249	−4.378
2° and 3°	−3.555	−3.585	−4.002	−4.032

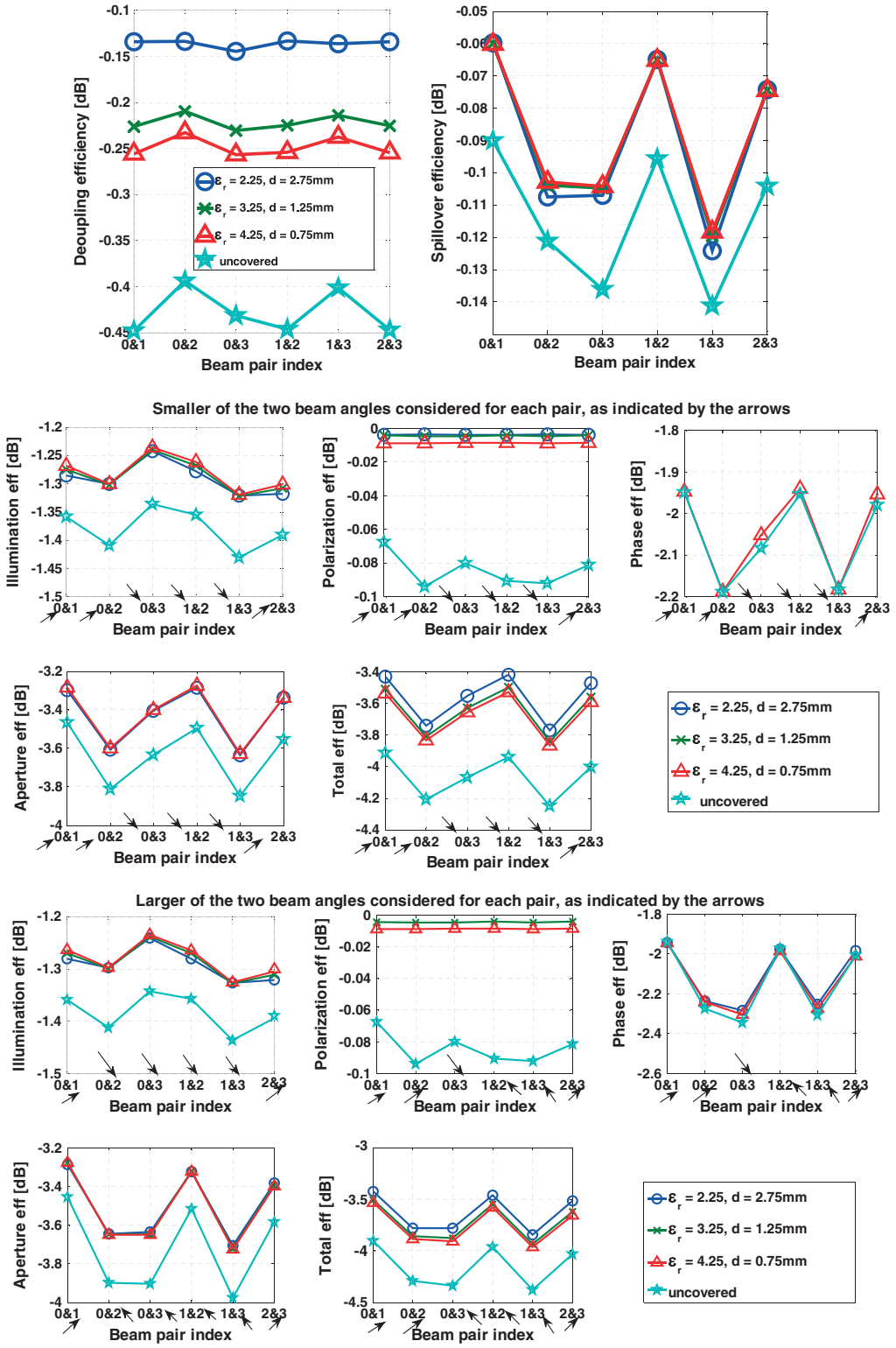

Figure 9. (a) Enhanced decoupling and spillover subefficiencies of a dual-beam parabolic reflector fed by three forms of dielectric-covered FPAs as compared to those of the uncovered counterpart for various beam pairs. These are common to both beam angles of every pair. The legend of the left side plot applies to both plots. (b) Individual beam subefficiencies of a dual-beam parabolic reflector fed by dielectric-covered FPAs for various beam pairs—enhanced over those of the uncovered counterpart. The data for the smaller of the two beam angles are indicated by the arrows. The larger case is given in Figure 9c. (c) Individual beam subefficiencies of a dual-beam parabolic reflector fed by the three best performing dielectric-covered FPAs for various beam pairs—enhanced over those of the uncovered counterpart. The data for the larger of the two beam angles are indicated by the arrows. The smaller case is given in Figure 9b.

effect of the decoupling efficiency on the overall performance, such that optimizing it translates to the maximization of the total efficiency, this time not only for just one beam but for both overlapping beams.

[60] It is observed from these results that for all except the decoupling subefficiency that is shared by both beams, the various efficiencies of the two individual beams are approximately equal at all slab conditions (ε_r, d) for every beam pair. In addition, it is seen that the optimum total and aperture efficiencies of the larger beam angle for every pair are generally slightly lower than those of the smaller one, which is as expected. Furthermore, upon comparing with the numerical data of the single scanned beam study in the preceding subsection for corresponding (ε_r, d) cases, the total efficiencies of the two constituent beams for each beam pair are found to be about 3 dB less than the total efficiencies of the respective solitary beams. Hence, a drop in the total efficiency by approximately 3 dB is generally sustained when an overlapping beam is added, since about half the injected energy is channeled into the other beam. Seen in another way, this fall is also as expected of the usual loss in gain with beam broadening when the main lobes of closely overlapping beams merge. The corresponding efficiency data for the same beam pairs radiated by the same 60° paraboloid of 5 m diameter but fed by uncovered FPAs are provided in Table 1. In addition to this optimal dielectric sheet, two other (ε_r, d) cases that provide among the greatest improvements are those of $\varepsilon_r = 3.25$ and $d = 1.25$ mm as well as $\varepsilon_r = 4.25$ and $d = 0.75$ mm. Extracting these cases, the enhancement is better presented graphically in Figures 9a–9c.

[61] Figure 9a shows the decoupling and spillover efficiencies of dual beams generated by the same 60° parabolic reflector of 5 m diameter fed by dielectric-covered FPAs for various beam pairs. As asserted in section 2.2.3, these two subefficiencies are shared by both constituent beams of any particular pair. The other subefficiencies of the aperture efficiency as well as the total efficiency are presented in Figures 9b and 9c for the smaller and larger beam angles of each beam pair, respectively. As explained in section 2.2.3, there is a set of aperture subefficiencies for every individual beam of each multiple (dual here) beam configuration. It can be observed from these figures that the dielectric covers can indeed significantly improve the total efficiencies of both constituent beams of all considered beam pairs as compared to those of the corresponding uncovered FPAs. Particularly, the enhancement for the best performer ($\varepsilon_r = 2.25$, $d = 2.75$ mm) is about 0.5 dB for every beam pair. As already explained, it is remarkable that the optimal dielectric cover configuration for overlapping dual beams is the same as when only a single steered beam is radiated, as seen from Figure 6. Hence, when the dielectric cover is optimized for single beam steering, it is also optimal for overlapping beams, which is greatly advantageous. This marks a vital discovery. Also, as asserted, it is shown that once a certain dielectric layer (of certain ε_r and d values) improves a beam pair (over the uncovered FPA counterpart), it also improves several, if not all, other beam pairs. This is also a key finding and further escalates the benefits offered by such dielectric covers placed over FPA feeds. As a final observation, when the angular separation between the beam pair is large, all aperture subefficiencies [of equation (2)] except the decoupling

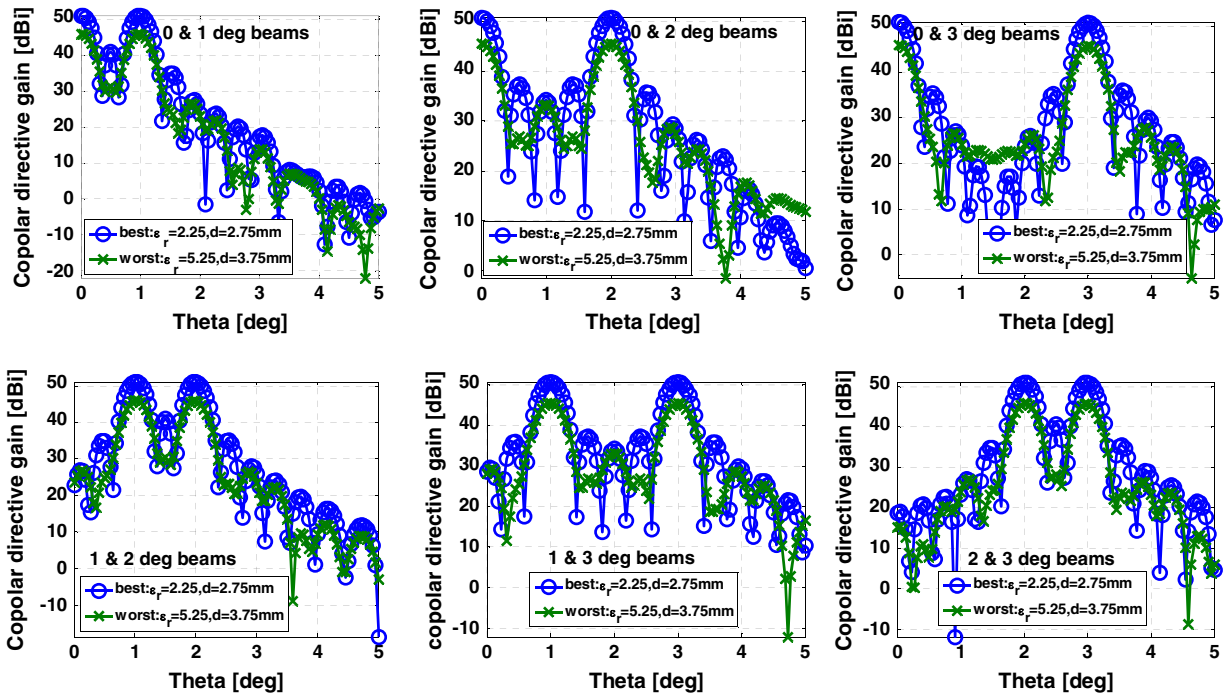

Figure 10. Co-polar directive gain patterns of various beam pairs for a 60° paraboloid of 5 m diameter fed by FPAs covered by a dielectric layer with ($\varepsilon_r = 2.25$, $d = 2.75$ mm) for the best performer and with ($\varepsilon_r = 5.25$, $d = 3.75$ mm) for the worst performer corresponding to circle and cross markers, respectively. The difference in directivity (toward beamed angle) between the best and worst performers equals the difference in their total efficiency.

efficiency of every constituent beam degrade as compared to when the beams are close together. This is exemplified by the dips and peaks in Figures 9b and 9c as well as the right side plot in Figure 9a for the spillover subefficiency. The decoupling efficiency of the left plot in Figure 9a is found to be unaffected by the beam separation. Therefore, we have demonstrated and uncovered another important finding: closely separated beams generally perform better than widely separated ones.

[62] The co-polar directive gain patterns of various beam pairs are presented in Figure 10 for both the best ($\varepsilon_r = 2.25$, $d = 2.75$ mm) and among the worst ($\varepsilon_r = 5.25$, $d = 3.75$ mm) performing dielectric covers. The six beam angle pairs are 0° and 1°, 0° and 2°, 0° and 3°, 1° and 2°, 1° and 3°, as well as 2° and 3°. As seen, the dual main beams are accurately produced along the two directions for every pair. The approximately 3 dB drop from the solitary main beam levels (about 54 dBi) in Figure 7 to around 51 dBi can be observed, as explained earlier to be coherent with efficiency loss associated with beam broadening and channeling of about half the injected power into the other beam. Also, as is the case for the single beams in Figure 7, the drop of about 5 dB in the main beam levels (for both beam angles, still in Figure 7) of any beam pair from the best to worst covers is approximately equal to the difference in the total efficiency between those two dielectric layers: drop in ε_{tot} from around −3.7 dB for the best sheet to about −8.7 dB for the worst. All these consistently logical phenomena serve as further validation of the work.

[63] The co-polar and cross-polar contour gain patterns of the overlapping 0° and 1° as well as 0° and 2° dual beams are presented in Figure 11. As before, these levels are shown with respect to the isotropic radiated power. It is clearly seen how the two strong lobes are accurately produced. Like

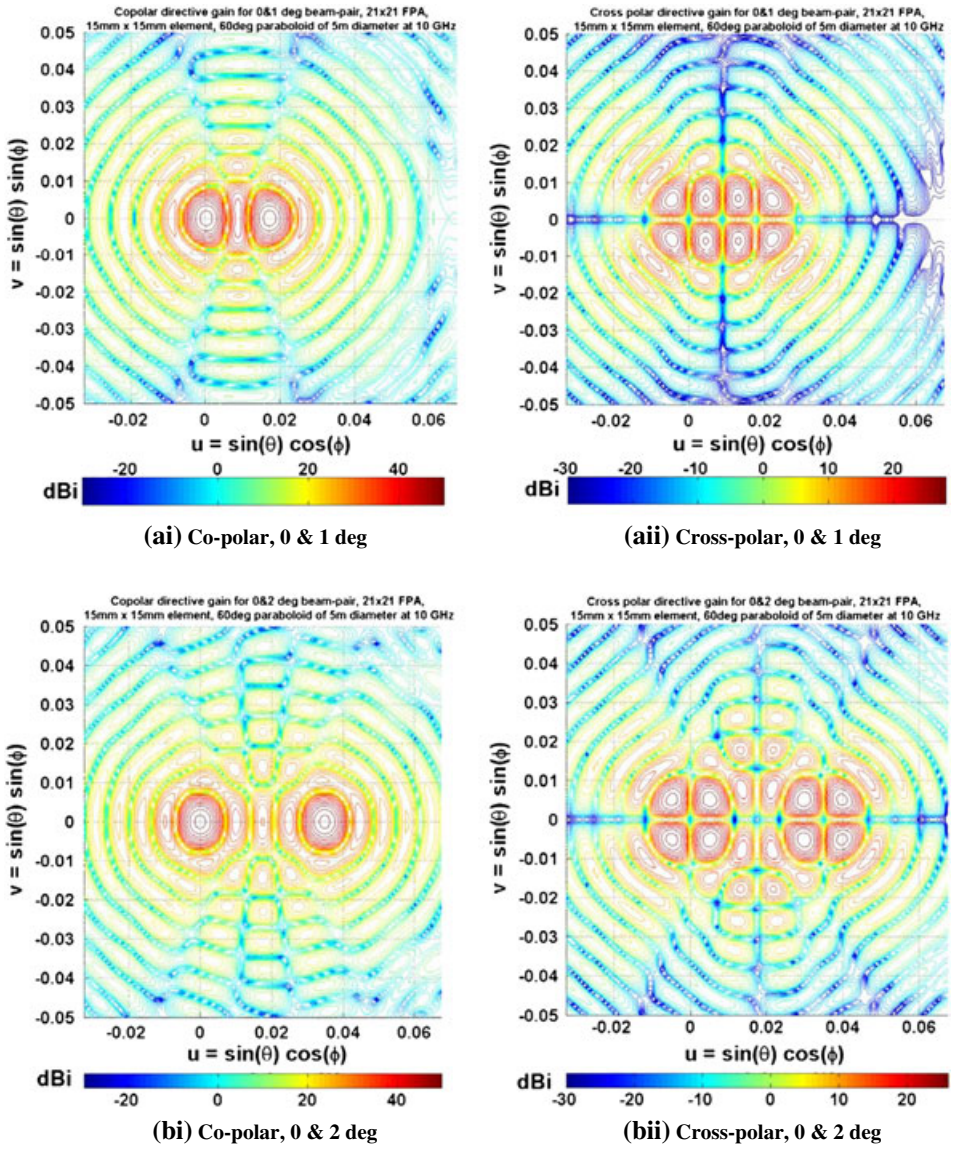

(ai) Co-polar, 0 & 1 deg

(aii) Cross-polar, 0 & 1 deg

(bi) Co-polar, 0 & 2 deg

(bii) Cross-polar, 0 & 2 deg

Figure 11. Contour gain plots with respect to the isotropic radiated power for the co-polar and cross-polar patterns: for (a) 0° and 1° and (b) 0° and 2° overlapping beams, for a 60° paraboloid with a 5 m diameter, fed by a dielectric-covered 21 × 21 FPA at 10 GHz, with $d_x = dy = \lambda/2$. For both beam pairs, the best performing cover ($\varepsilon_r = 2.25$, $d = 2.75$ mm) is considered.

previously, the four diagonal cross-polar lobes surrounding each constituent main beam can be noticed. The peak cross-polar levels are again noted to be at least around 20 dB below the maximum co-polar levels of their respective main beams.

[64] The reasons why dielectric-covered FPA feeds can achieve efficiency enhancement of single off-axis and multiple overlapping beam reflectors are two pronged. First, the decoupling efficiency has been found to be the most crucial and singularly influential factor on the overall performance (see Figure 5), demonstrating the greater importance of operating at the maximum of the decoupling efficiency than optimizing any other subefficiencies. It encompasses mutual coupling and reflection losses throughout the FPA. Hence, the dielectric slab serves as a form of impedance matching layer. Second, the dielectric cover opens up to infinite degrees of freedom with unlimited possible combination pairs of slab parameters (ε_r, d), in stark contrast to just one specific condition ($\varepsilon_r = 1$, $d = \infty$) for the case without any slab cover.

5. Various Reflector Configurations

[65] In addition to the specific case of parabolic reflectors studied in the preceding section, having a half-subtended angle of 60° and a diameter of 5 m, various other configurations shall be investigated in this section. Specifically, permutations of dish angles of 30°, 45°, and 60° in connection with diameters of 2.5, 5, and 7.5 m are also studied. The same FPA properties as before are retained here, as in the same 21×21 array population of half-wavelength-sized unit cells encompassing identical radiating apertures, with the same buffer elements surrounding the excited portion of the array.

[66] Figure 12 presents several graphs of the optimum total efficiency with beam angle for various combinations of dish angle and diameter. Each subplot in the upper row gives the variation of the maximum total efficiency with beam angle for a certain dish diameter, each trace within it pertaining to a particular dish angle, with its associated (ε_r, d) dielectric slab condition as indicated. The same data are replotted in the lower row of graphs in the same figure, but with the dish diameters and angles swapped, i.e., each subplot in the lower row is for a certain dish angle, with every parametric trace corresponding to a certain diameter. Astoundingly, a universal optimal $\varepsilon_r = 2.25$ is observed, regardless of the dish angle and diameter. The upper row plots reveal that the optimum slab depth rises with increasing dish angle. The plots in the lower row demonstrate the invariance of the optimum slab conditions with the dish diameter for any dish angle. This means that the optimal dielectric cover varies only with the dish angle (particularly, only its depth rises with it) and does not depend on the diameter. This marks yet another monumental discovery.

6. Conclusions

[67] The growing prospects that FPA feeds have on enhancing the performance of modern reflectors play an important role in the progress of satellite communications and radiotelescope technology. Due to the obvious benefits of retaining a single stationary reflector antenna, such robust feeds offer strong advantages in terms of scan range, continuity of enlarged field of coverage, ability to provide services to widely separated locations on earth, and flexibility in achieving rapidly varying contoured footprints. For these reasons, a

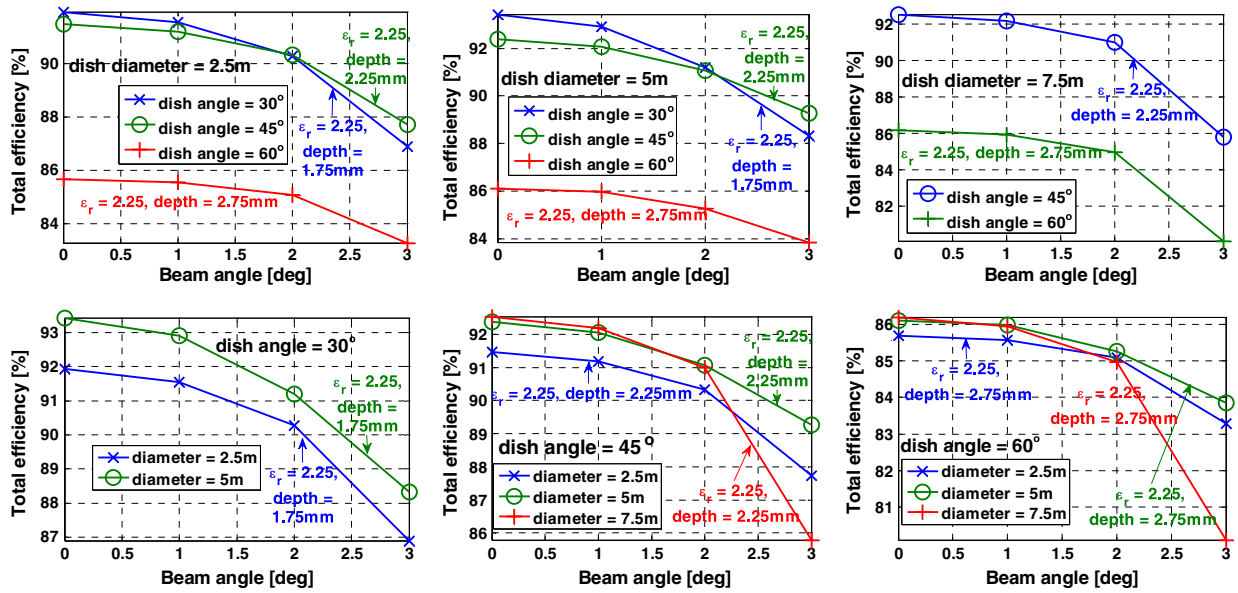

Figure 12. Each subplot in the upper row gives the variation of optimum total efficiency with beam angle for a certain dish diameter, each trace pertaining to a particular dish angle, with its associated (ε_r, d) dielectric slab condition as indicated. The same data are replotted in the lower row of graphs, but with swapping dish diameters and angles, i.e., each subplot for a certain dish angle, with diameter as a parametric trace. The universal optimal $\varepsilon_r = 2.25$ was discovered, regardless of dish angle and diameter. The upper row reveals increasing optimum slab depth with increasing dish angle. The lower row shows invariance of optimum slab conditions with dish diameter for any dish angle.

dedicated investigation into ways of further improving the capabilities of FPA feeds is justified. This work has looked into and successfully demonstrated the ability of dielectric covers placed over FPA feeds comprising waveguide elements to achieve improved total efficiencies of single steered as well as multiple overlapping beams, as compared to those of uncovered FPA feeds. It is shown that the decoupling efficiency of the FPA feed is an important factor for complete and accurate characterization of the entire FPA-fed reflector system. Furthermore, we have aptly emphasized the importance of considering not only one or a few subefficiencies but the entire set constituting the total efficiency. Another significant finding is that when a dielectric cover is optimal for a single steered beam, it also performs the best for multiple overlapping beams. In addition, whenever a slab cover enhances a pair of beams, it would also improve other pairs. All these provide vast benefits. An important aspect learned is that beams close together generally perform better than widely separated ones. Finally, a bandwidth study shows that the performance enhancement afforded by dielectric covers could enjoy bandwidths that could reach as high as nearly 10%.

[68] **Acknowledgment.** This work was supported by the National Science Council of Taiwan.

References

Amitay, N., V. Galindo, and C. P. Wu (1972), Theory and Analysis of Phased Array Antennas, Wiley Interscience, New York.

Balling, P. (1987), Spacecraft multi-beam and contoured-beam antennas, AGARD Microwave Antennas for Avionics.

Brisken, A. F., R. E. Anderson, R. L. Frey, and J. R. Lewis (1979), Land mobile communications and position fixing using satellites, *IEEE Trans. Veh. Technol.*, *28*(3), 153–174.

Egami, S. (1987), An adaptive multiple-beam transmitter for satellite communications, *IEEE Trans. Aerosp. Electron. Syst.*, *23*(1), 11–16.

Egami, S. (1999), A power-sharing multiple beam mobile satellite in Ka band, *IEEE J. Sel. Areas Commun.*, *17*(2), 145–152.

Hwang, Y. (1992), Satellite antennas, *Proc. IEEE*, *80*(1), 183–193.

Jorgensen, R., and P. Balling (1985), Dual offset reflector multibeam antenna for international communications satellite applications, *IEEE Trans. Antennas Propag.*, *33*(12), 1304–1312.

Kildal, P.-S. (2000), Foundations of Antennas, Studentlitteratur, Lund, Sweden.

Kreutel, R. W., Jr., D. F. DiFonzo, W. J. English, and R. W. Gruner (1977), Antenna technology for frequency reuse satellite communications, *Proc. IEEE*, *65*(3), 370–378.

Ng Mou Kehn, M., and P.-S. Kildal (2005), Miniaturized rectangular hard waveguides for use in multifrequency phased arrays, *IEEE Trans. Antennas Propag.*, *53*(1), 100–109.

Ng Mou Kehn, M., M. Nannetti, A. Cucini, S. Maci, and P.-S. Kildal (2006), Analysis of dispersion in dipole-FSS loaded hard rectangular waveguide, *IEEE Trans. Antennas Propag.*, *AP-54*(8), 2275–2282.

Ng Mou Kehn, M., and L. Shafai (2008), Characterization of dense focal plane array feeds for parabolic reflectors in achieving closely-overlapping or widely-separated multiple beams, *Radio Sci.*, doi:10.1029/2008RS003953.

Ng Mou Kehn, M., and L. Shafai (2009), Improved matching of waveguide focal plane arrays using patch array covers as compared to conventional dielectric sheets, *IEEE Trans. Antennas Propag.*, *57*(10), 3062–3076.

Rao, S. M., D. R. Wilton, and A. W. Glisson (1982), Electromagnetic scattering by surfaces of arbitrary shape, *IEEE Trans. Antennas Propag.*, *AP-30*(3), 409–418.

Sipus, Z. (1997), Analysis of planar and circular cylindrical multilayer structures with application to soft and hard surfaces, Technical Report no. 317, Chalmers University of Technology, Sweden, PhD Thesis.

Sipus, Z., P.-S. Kildal, R. Leijon, and M. Johansson (1998), An algorithm for calculating Green's functions of planar, circular cylindrical, and spherical multilayer structures, *ACES J.*, *13*(3), 243–254.

Wu, W. W., E. F. Miller, W. L. Pritchard, and R. L. Pickholtz (1994), Mobile satellite communications, *Proc. IEEE*, *82*(9), 1431–1448.

Zaghloul, A. I., Y. Hwang, R. M. Sorbello, and F. T. Assal (1990), Advances in multibeam communications satellite antennas, *Proc. IEEE*, *78*(7), 1214–1232.